



Article

Airborne Elevation DBF-TOPS SAR/InSAR Method Based on LOS Motion Compensation and Channel Error Equalization

Zhiyong Suo ^{1,*}, Jingjing Ti ¹, Hongli Xiang ^{1,2}, Leru Zhang ¹, Chao Xing ¹ and Tingting Wang ^{1,2}¹ National Laboratory of Radar Signal Processing, Xidian University, Xi'an 710071, China² Sichuan Aerospace Electronic Equipment Research Institute, Chengdu 610100, China

* Correspondence: zysuo@xidian.edu.cn; Tel.: +86-29-8820-2248

Abstract: Digital beamforming (DBF) TOPS SAR in elevation is a new synthetic aperture radar (SAR) system, which has the advantage of wide swath coverage and a high signal-to-noise ratio (SNR). In this paper, considering the phase preservation demand for interferometric SAR (InSAR) processing, the complete processing chain for DBF-TOPS SAR/InSAR in elevation is proposed with a wide beam angle and channels' amplitude and phase errors. Firstly, we analyze the airborne motion compensation method along the line-of-sight direction for TOPS SAR with squint angle. Furthermore, for the large-range beam angle of DBF, the sub-swaths division process is presented for the range-dependent radar look angle, and the sub-swaths division criterion is also given in the analytic expression. Then, the relative amplitude and phase errors' estimation and compensation method between channels is provided in the range frequency domain based on the pivoting filter with coherence weighting, which is convenient for DBF processing and SNR improvement. Finally, the DEMs are generated under different conditions to compare the phase preservation performance. The effectiveness of the proposed processing chain is verified with both simulated data and airborne real DBF-TOPS SAR/InSAR data.



Citation: Suo, Z.; Ti, J.; Xiang, H.; Zhang, L.; Xing, C.; Wang, T. Airborne Elevation DBF-TOPS SAR/InSAR Method Based on LOS Motion Compensation and Channel Error Equalization. *Remote Sens.* **2022**, *14*, 4542. <https://doi.org/10.3390/rs14184542>

Academic Editor: Stefano Tebaldini

Received: 7 August 2022

Accepted: 8 September 2022

Published: 11 September 2022

Publisher's Note: MDPI stays neutral with regard to jurisdictional claims in published maps and institutional affiliations.



Copyright: © 2022 by the authors. Licensee MDPI, Basel, Switzerland. This article is an open access article distributed under the terms and conditions of the Creative Commons Attribution (CC BY) license (<https://creativecommons.org/licenses/by/4.0/>).

Keywords: digital beamforming (DBF) in elevation; terrain observation by progressive scans SAR (TOPS SAR); motion compensation (MoCo); channel equalization

1. Introduction

High-resolution wide swath (HRWS) synthetic aperture radar (SAR) is a future research focus. The multi-channel technique is an effective technique for HRWS SAR imaging [1–4]. Beam-steering SARs, including ScanSAR [5] and terrain observation by progressive scans (TOPS) SAR [6], are often used for wide swath observation nowadays. However, for the wide swath scanning, the radar beam dwell time of beam-steering SAR is reduced compared to the stripmap SAR and the spotlight SAR [7]. Therefore, the signal-to-noise ratio (SNR) of a focused SAR image will be decreased in the beam-scanning SAR systems. Due to the SNR loss, the processing performance of some applications, including ground-moving target indication (GMTI) [8], radar target classification [9], and interferometric SAR (InSAR) [10], will inevitably be deteriorated. HRWS SAR with high SNR is an important trend for future SAR systems. Therefore, we will focus on the elevation DBF-TOPS SAR/InSAR processing method to improve the SNR in this paper.

As is known, TOPS SAR mode was first provided in [6]. Furthermore, the spaceborne-based TOPS SAR mode is verified with TerraSAR-X, and the extended chirp scaling (ECS) algorithm is used to focus the SAR echoes [11]. The experiment proved that the TOPS SAR image eliminates the scalloping modulation in the ScanSAR image. Then, the InSAR experiment was also executed in [12]. In 2014, Sentinel-1A was launched, and it was the first satellite taking TOPS as its main working mode [13].

The imaging methods of single-channel TOPS SAR and azimuth multi-channel TOPS SAR have been extensively investigated. For the azimuth multi-channel system, the SNR

improvement is intrinsically obtained by the increased sampling numbers [14]. For the beam-steering SAR, some methods have been investigated to formulate the motion displacement model, and then the motion compensation methods were also developed for well-focused SAR image formulation. The moving band chirp Z-transform in the wavenumber domain for TOPS SAR with full-aperture focusing is proposed, which avoids up-sampling or sub-aperture processing [15]. The full-aperture SAR imaging method is also proposed in [16] by using a slightly larger pulse repetition frequency (PRF) over the instantaneous bandwidth, which can be used for both sliding spotlight SAR and TOPS SAR. To equalize SNR for TOPS SAR images, the radar beam-steering rate is set nonuniformly [17]. In [18], multi-channel TOPS SAR in azimuth is designed, and the channel mismatch cancellation and unambiguous signal reconstruction method are given for ultrawide-swath imaging with high spatial resolution. The modified full-aperture imaging algorithm with zero substitution between bursts is investigated for sliding mosaic mode synthetic SAR imaging [19]. The improved frequency scaling algorithm is proposed with de-rotation operation to remove the aliasing in the azimuth time domain for TOPS SAR full-aperture imaging in [20]. The multiple-input multiple-output (MIMO) SAR system is also designed for multimodal operation, simultaneously including the wide swath imaging, sliding spotlight, and highly sensitive GMTI [21]. The SAR imaging algorithm and autofocus processing of the automobile forward-looking MIMO SAR system are investigated in [22] with residual velocities' estimation by ground control points (GCP).

DBF-SAR is widely investigated, especially for the stripmap mode. Generally, DBF is executed by array antennas. Compensating for the wave path difference or phase difference, DBF in elevation achieves the coherent integration of the received signals to improve SNR [23]. That is to say, the maximal power will be reached in a certain direction with DBF. DBF is widely used in radar and communication fields. The digital beamforming synthetic aperture radar (DBSAR) system is designed and experimentalized for multimode measurements by National Aeronautics and Space Administration (NASA), and the DBSAR system verifies the multi-function in a single radar platform [24–26]. The spaceborne DBF-SAR in elevation is executed by the TerraSAR-X satellite, which shows the better SNR images than the single-channel SAR system [27]. The null steering technique combining with DBF in elevation is employed for linear frequency modulation (LFM)-based MIMO SAR processing without channel error consideration [28]. By using the spaceborne-stationary bistatic configuration, the elevation DBF-SAR experiment with TerraSAR-X as an illuminator is executed. However, the working mode is the stripmap mode [29]. Assuming that the received signals come from different angles and have sparsity in the spatial domain, the sparse-based direction of arrival (DOA) estimation is performed to estimate the weighted vector for DBF [30]. A new multiple-elevation beam SAR system to reduce the echo data amount is provided with multiple sub-pulses' transmission, and the focus processing scheme with a coarse digital elevation model (DEM) is also presented [31]. The posture error compensation method combined with motion compensation for the two-dimensional (2D) array antenna is proposed in [32], where the position error caused by the posture error with stripmap SAR mode is thoroughly discussed [32]. The nadir echoes effect on SAR images in multiple elevation-beam SAR is investigated with different PRF settings, and the effect is verified by the TerraSAR-X data-based simulations [33]. The airborne X-Band SAR system with 16 channels in elevation is used for HRWS SAR imaging, and the channel mismatch processing and the pattern loss compensation are also considered for SNR improvement of the SAR image [34]. The effect of terrain height and pulse length on the multibeam of scan-on-receive (SCORE) SAR is detailed and analyzed by simulation results [35].

Motion compensation (MoCo) is the key step in the airborne SAR imaging [36–39] and the ISAR imaging [40–42] because of the nonstationary motion of the platform. Most MoCo methods compensate the motion displacement with the zero-Doppler motion error. The line-of-sight (LOS) MoCo is proposed for very high-resolution SAR in [43]. However, the proposed LOS MoCo only considers the zero-Doppler centroid mode, and the squint

mode is not investigated. Furthermore, the phase gradient auto-focus [44] (PGA) is used to improve the focusing performance in the azimuth direction. Since PGA estimates the residual motion error from SAR echoes rather than the inertial measurement unit (IMU), the real SAR imaging geometry will be lost, and then the phase preservation performance will be deteriorated. In [45], the modified extended-range migration algorithm (ERMA) method is proposed for the airborne platform's maneuverability with squint angle, and the residual phase error caused by acceleration is calibrated with two-step processing. The range processing of the near-nadir TOPS SAR system without blocks' division is proposed in [46]. However, the phase preservation performance is still never discussed in the above works.

From the analysis and review above, we can see that TOPS SAR imaging has been extensively investigated, and DBF-SAR in elevation has also been deeply investigated for stripmap SAR. The focusing performance is well done within the previous works. However, the phase preservation performance has been seldom investigated, which is very important for InSAR processing. Actually, phase preservation indicates the SAR imaging geometry's accuracy. For InSAR processing, the principal phase value is obtained by the 2π module of slant range. Therefore, if the principal phase value cannot be accurately obtained, it will lead to InSAR fringes' distortion. Furthermore, because of the reduced beam dwell time of TOPS SAR, the SNR will be decreased, which is one of the key factors for InSAR fringes and DEM generation with height accuracy. The future work for ocean observation also needs wide swath coverage and high SNR images [47]. Combined with multi-channel DBF in elevation, the SAR image's SNR will be improved. Therefore, the new SAR system combining the advantages of TOPS SAR and DBF in elevation simultaneously on the airborne platform should be intensively studied to obtain high SNR SAR images with wide swath. Based on the analysis, we will focus on the processing flowchart for the airborne elevation DBF-TOPS SAR/InSAR in this paper. The presented flowchart mainly includes single-channel DBF-TOPS SAR motion compensation with a wide beam angle and squint angle, channel errors' estimation for DBF-TOPS SAR in elevation, and DBF-TOPS InSAR DEM generation.

The paper is arranged as follows. In Section 2, the main principles and methods for DBF-TOPS SAR processing are discussed. Firstly, we describe the signal model of DBF SAR in elevation. Secondly, by considering the phase preservation performance, we analyze the single-channel airborne TOPS SAR motion compensation method along the line-of-sight (LOS), with a wide beam-scanning angle and squint angle. Furthermore, the processing strategy of the range-dependent radar look angle for DBF is also presented. Thirdly, the elevation channel error estimation and compensation with coherence-weighted filter is provided. Based on the analysis above, the complete flowchart of the airborne elevation DBF-TOPS SAR imaging method is given in detail in Section 2.4. The performance investigation of DBF-TOPS SAR/InSAR is presented in Section 3 with both simulated and real airborne data. Some discussions are presented for the new DBF-TOPS SAR system investigation in Section 4. Summarization of the whole paper is presented in the final section.

2. Principles and Methods for DBF-TOPS SAR in Elevation

2.1. Signal Model of DBF-TOPS SAR in Elevation

2.1.1. Time Delay Analysis of Linear Array Antennas

For simplicity, the geometric model of multi-channel DBF-TOPS SAR in elevation is shown in Figure 1a. The system consists of one transmitting antenna and three receiving antennas. The transmitting channel is used to form a wide-range-covering antenna pattern, and the receiving channels receive radar echoes simultaneously. In Figure 1a, the transmitting and receiving antennas do not coincide. That is to say, the positions of transmitting antenna centers and receiving antenna centers are different. Therefore, the total slant range of point P from the transmitting antenna to one receiving antenna (taking Rx3 as an example) equals $R_T + R_{Rx3}$, which leads to the difficulty in analyzing the radar echoes in the frequency domain [48]. If the distance between the middle position of the

transmitting antenna center and the receiving antenna center to point P is defined as R_{EPC3} , then the phase difference term calculated from $R_T + R_{Rx3} - 2R_{EPC3}$ is compensated to the radar echoes. Therefore, the transmission and reception positions coincide. The middle position is called the equivalent phase center (EPC). In the paper, the channel positions refer to the EPCs' positions, whenever the radar works with bistatic geometry and/or monostatic geometry.

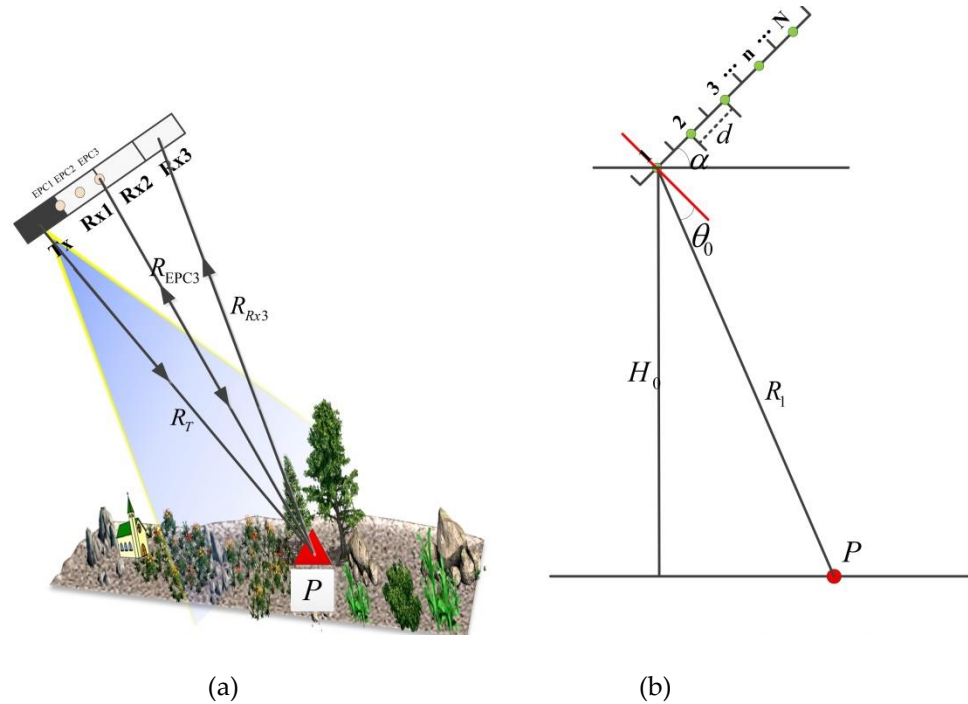


Figure 1. Geometric model of DBF-SAR in elevation. (a) EPC model. (b) DBF-SAR model.

With EPC equivalence, the universal geometry of DBF in elevation with linear array is shown in Figure 1b, where we assume that there are N channels, the distance between adjacent antenna phase centers is d , the inclination angle of the linear antenna array is α , H_0 is the height of the reference channel, R_1 is the slant range between the reference channel and the point P , and θ_0 is the angle of linear array and its normal line. Then, the DOA of point P is expressed as follows:

$$\theta_0 = \arccos(H_0/R_1) - \alpha \tag{1}$$

DOA in the range direction can be expressed as:

$$\theta(\xi) = \arccos(2H_0/c\xi) - \alpha \tag{2}$$

where ξ is the time delay in the range direction.

With the definition of R_1 , the slant range R_n between point P and the n th antenna is expressed as:

$$R_n = \sqrt{R_1^2 + d_n^2 - 2 \cdot R_1 \cdot d_n \cos(\frac{\pi}{2} + \theta_0)} = \sqrt{R_1^2 + d_n^2 + 2 \cdot R_1 \cdot d_n \sin \theta_0} \tag{3}$$

$$\approx R_1 + d_n \sin \theta_0 + \frac{d_n^2}{2R_1}$$

where $d_n = (n - 1)d$ is the distance between the channel n and the reference channel. Generally, $d_n \ll R_1$, then (3) can be approximately expressed as:

$$R_n \approx R_1 + d_n \sin \theta_0 = R_1 + (n - 1)d \sin \theta_0 \tag{4}$$

If the time delay of the reference channel is $\tau_1 = 2R_1/c$, then the time delay of channel n is:

$$\tau_n = \frac{R_1 + R_n}{c} = \tau_1 + \frac{(n-1)d \sin \theta_0}{c} \quad (5)$$

2.1.2. Signal Model of DBF-TOPS SAR

The radar transmits an LFM signal:

$$s_t(\tau) = \text{rect}\left(\frac{\tau}{T}\right) \exp(j2\pi f_c \tau + j\pi K_r \tau^2) \quad (6)$$

where $j = \sqrt{-1}$, τ represents the range time, f_c is the central frequency, K_r is the range chirp rate, T is the pulse duration time, and $\text{rect}(\cdot)$ is the normalized rectangle window:

$$\text{rect}(t) = \begin{cases} 1, & |t| \leq 0.5 \\ 0, & |t| > 0.5 \end{cases} \quad \text{with } t = \tau/T \quad (7)$$

The radar echo of the n th channel is expressed as:

$$s_n(\tau) = A_0 \cdot \text{rect}\left(\frac{\tau - \tau_n}{T}\right) \exp(j2\pi f_c(\tau - \tau_n) + j\pi K_r(\tau - \tau_n)^2) \quad (8)$$

where A_0 is the amplitude of radar echoes. Then, the baseband radar echoes are shown as:

$$\begin{aligned} s_n(\tau) &= A_0 \cdot \text{rect}\left(\frac{\tau - \tau_n}{T}\right) \exp(-j2\pi f_c \tau_n + j\pi K_r(\tau - \tau_n)^2) \\ &= A_0 \cdot \text{rect}\left(\frac{\tau - (\tau_1 + \Delta\tau_n)}{T}\right) \exp(-j2\pi f_c(\tau_1 + \Delta\tau_n) + j\pi K_r(\tau - (\tau_1 + \Delta\tau_n))^2) \end{aligned} \quad (9)$$

where $\Delta\tau_n = \frac{(n-1)d \sin \theta_0}{c}$. If $\Delta\tau_n \cdot c < \rho_r/8$ (ρ_r is the slant range resolution), then the envelopes' distortion of different channels caused by $\Delta\tau_n$ can be ignored. Therefore, all the channels have the same envelopes. However, if $\Delta\tau_n \cdot c \geq \rho_r/8$, then the envelopes should be registered to the reference channel. It should be emphasized that the phase deviations, $\exp(-j2\pi f_c \Delta\tau_n)$, caused by $\Delta\tau_n$ cannot be ignored in any circumstance, and should be compensated necessarily and accurately, especially for InSAR processing.

If the DOA of point P is θ_0 , then the steering vector of point P for DBF can be expressed as:

$$\mathbf{a}(\theta_0) = \left[1, \exp(-j\frac{2\pi}{\lambda} d \sin \theta_0), \exp(-j\frac{2\pi}{\lambda} \cdot 2d \sin \theta_0), \dots, \exp(-j\frac{2\pi}{\lambda} \cdot (N-1)d \sin \theta_0) \right] \quad (10)$$

The steering vector for a given point in the range direction can be expressed as:

$$\mathbf{w}(\tau) = \left[1, \exp(j\frac{2\pi}{\lambda} d \sin(\theta(\tau))), \exp(j\frac{2\pi}{\lambda} 2d \sin(\theta(\tau))), \dots, \exp(j\frac{2\pi}{\lambda} (N-1)d \sin(\theta(\tau))) \right] \quad (11)$$

Finally, the output of DBF SAR is given below:

$$s_{DBF}(\tau) = \sum_{n=1}^N w_n(\tau) \cdot s_n(\tau) \quad (12)$$

where $w_n(\tau)$ is the n th weight coefficient of $\mathbf{w}(\tau)$.

2.2. Motion Displacement Analysis and Compensation of DBF-TOPS SAR along Line-of-Sight

2.2.1. Motion Displacement Model and Azimuth Variation Analysis of TOPS SAR

The airborne TOPS SAR geometric model with motion displacement is shown in Figure 2. The flight path of the radar platform is unstable due to the influence of air flow. Therefore, the real track will be deviated from the ideal track (dashed straight line). The beam center line is steered to point P .

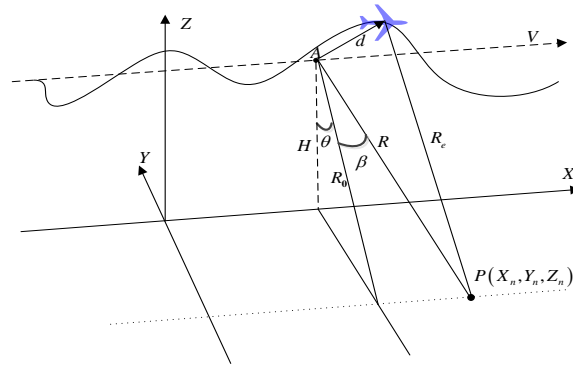


Figure 2. Radar motion displacement model of TOPS SAR.

The coordinates of point P are (X_n, Y_n, Z_n) , the platform moves along the X -axis, t_m is the azimuth time, $[x(t_m), 0, H]$ is the ideal position at t_m , and $[\Delta x(t_m), \Delta y(t_m), \Delta z(t_m)]$ are the position displacements at t_m ; then, the actual position of the platform is $[x(t_m) + \Delta x(t_m), \Delta y(t_m), H + \Delta z(t_m)]$. β is the squint angle between the equivalent antenna phase center (APC) and the target at t_m , θ is the radar look angle, $R_0 = \sqrt{Y_n^2 + (H - Z_n)^2}$ is the nearest slant range between the target and the ideal track, and $Y_n = -R_0 \cdot \sin \theta$, $H - Z_n = R_0 \cdot \cos \theta$, and $R(t_m)$ is the instantaneous slant range with the ideal track and can be expressed as:

$$R(t_m) = \sqrt{(x(t_m) - X_n)^2 + Y_n^2 + (H - Z_n)^2} \quad (13)$$

The instantaneous slant range with motion displacements is shown as:

$$R_e(t_m) = \sqrt{(x(t_m) + \Delta x(t_m) - X_n)^2 + (\Delta y(t_m) - Y_n)^2 + (H + \Delta z(t_m) - Z_n)^2} \quad (14)$$

Combining (13) and (14), we obtain:

$$\begin{aligned} R_e(t_m) &= \sqrt{(x(t_m) + \Delta x(t_m) - X_n)^2 + (\Delta y(t_m) - Y_n)^2 + (H + \Delta z(t_m) - Z_n)^2} \\ &= \sqrt{(x(t_m) - X_n)^2 + Y_n^2 + (H - Z_n)^2 + 2(x(t_m) - X_n) \Delta x(t_m) + \Delta x^2(t_m) - 2Y_n \Delta y(t_m) + \Delta y^2(t_m) + 2(H - Z_n) \Delta z(t_m) + \Delta z^2(t_m)} \\ &= \sqrt{R^2(t_m) + 2(x(t_m) - X_n) \Delta x(t_m) + \Delta x^2(t_m) - 2Y_n \Delta y(t_m) + \Delta y^2(t_m) + 2(H - Z_n) \Delta z(t_m) + \Delta z^2(t_m)} \\ &\approx R(t_m) + \frac{x(t_m) - X_n}{R(t_m)} \Delta x(t_m) - \frac{Y_n}{R(t_m)} \Delta y(t_m) + \frac{(H - Z_n)}{R(t_m)} \Delta z(t_m) \end{aligned} \quad (15)$$

Then, the slant range error is:

$$\begin{aligned} \Delta R(t_m) &= \frac{x(t_m) - X_n}{R(t_m)} \Delta x(t_m) - \frac{Y_n}{R(t_m)} \Delta y(t_m) + \frac{(H - Z_n)}{R(t_m)} \Delta z(t_m) \\ &\approx \frac{x(t_m) - X_n}{R(t_m)} \Delta x(t_m) + \cos \beta (\Delta y(t_m) \cdot \sin \theta + \Delta z(t_m) \cdot \cos \theta) \end{aligned} \quad (16)$$

where $\frac{x(t_m) - X_n}{R(t_m)} \Delta x(t_m)$ is the motion displacement in azimuth (along track), and $\cos \beta (\Delta y(t_m) \cdot \sin \theta + \Delta z(t_m) \cdot \cos \theta)$ is the motion displacement in the vertical plane perpendicular to the track along the slant range direction. We can see that the motion displacements vary with both θ and β during the TOPS SAR imaging. Then, the radar echoes with motion displacements are expressed as:

$$\begin{aligned} s_r(t_m, \tau) &= A w_r \left\{ \tau - \frac{2[R(t_m) + \Delta R(t_m, \tau)]}{c} \right\} w_a(t_m - t_c) \cdot \\ &\quad \exp \left[-j4\pi \frac{R(t_m) + \Delta R(t_m, \tau)}{\lambda} \right] \exp \left\{ j\pi K_r \left[\tau - \frac{2[R(t_m) + \Delta R(t_m, \tau)]}{c} \right]^2 \right\} \end{aligned} \quad (17)$$

In practice, the ideal track is fitted by the measured data from the instrument SPAN-CPT5, which is a high-accuracy instrument integrated Global Navigation Satellite System (GNSS) and integrated navigation system (INS), and it can provide the radar information

with positions, velocities, and postures in three-dimension (3D). Therefore, the radar phase center can be calculated from the parameters. For SAR data acquisition, the 3D geometry is projected to the 2D plane (named the slant range plane, see Figure 3), which is generally defined by the ideal track and the radar beam center line. Therefore, the 3D motion displacements in the Cartesian coordinate system can be decomposed into other 3D coordinates, i.e., azimuth direction (X axis), slant range direction, and normal direction of the slant range plane. The motion displacement of the normal direction has no projection component along the slant range direction, and therefore it will not affect the SAR focusing performance. Then, the motion compensation is executed to compute the displacement between the real track (i.e., the measured parameters) and its projection position to the ideal track in the 2D plane, i.e., ΔR in Figure 3. We called this the narrow-band (NB MoCo) assumption in this paper. For the TOPS-SAR motion displacements shown in Figure 3 with squint angle, the slant range error is azimuth-variant for different points in the same range cell.

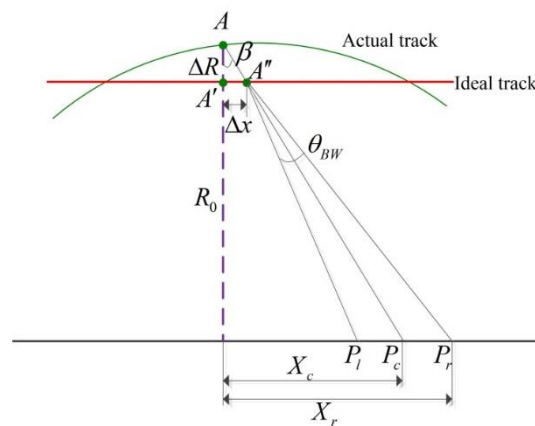


Figure 3. Azimuth motion displacement variation model.

In the following, we will analyze the motion displacement variation characteristics in azimuth of TOPS SAR with squint angle. In Figure 3, A , A' , and A'' are the platform positions on the actual track, the projection position of A on the ideal track, and the cross-point of the ideal track and the line-of-sight at t_m , respectively. P_l , P_c , and P_r are the points at the left edge of the radar beam, in the center of the radar beam, and at the right edge of the radar beam, respectively. ΔR is motion displacement referenced to the nearest slant range. Therefore, we have the following two equations:

$$\Delta x = \Delta R \cdot \tan \beta \tag{18}$$

$$X_r = \Delta x + R_0 \cdot \tan(\beta + \theta_{BW}/2) \tag{19}$$

where Δx is the distance between A' and A'' , θ_{BW} is the beam width in azimuth, and X_r and X_c are the azimuth coordinates relative to the zero-Doppler position when the platform position is at point A .

By using the conventional narrow-beam compensation method, the slant range error of P_c is shown below:

$$\Delta R_{c,1} = \left| \vec{AP}_c \right| - \left| \vec{A''P}_c \right| = \sqrt{(R_0 + \Delta R)^2 + X_c^2} - \sqrt{R_0^2 + X_c^2} \tag{20}$$

The slant range error of P_r is:

$$\begin{aligned} \Delta R_{r,1} &= \left| \vec{AP}_r \right| - \left| \vec{A''P}_r \right| = \sqrt{(R_0 + \Delta R)^2 + X_r^2} - \sqrt{R_0^2 + X_r^2} \\ &\approx \sqrt{(R_0 + \Delta R)^2 + \left(X_c + R_0 \cdot \frac{\theta_{BW}}{2} \right)^2} - \sqrt{R_0^2 + \left(X_c + R_0 \cdot \frac{\theta_{BW}}{2} \right)^2} \end{aligned} \tag{21}$$

Compared to P_c , the residual slant range error of P_r is:

$$\begin{aligned}\Delta R_{resr,1} &= \Delta R_{r,1} - \Delta R_{c,1} \\ &= \sqrt{(R_0 + \Delta R)^2 + \left(X_c + R_0 \cdot \frac{\theta_{BW}}{2}\right)^2} - \sqrt{R_0^2 + \left(X_c + R_0 \cdot \frac{\theta_{BW}}{2}\right)^2} \\ &\quad - \left(\sqrt{(R_0 + \Delta R)^2 + X_c^2} - \sqrt{R_0^2 + X_c^2}\right)\end{aligned}\quad (22)$$

In the following simulation, we can see that the residual slant range error cannot be ignored during the TOPS SAR imaging, especially for the demand of the phase reservation performance of InSAR. Therefore, the slant range error compensation method along LOS with squint angle should be used. If the slant range error is computed along LOS, then the slant range error of P_c is:

$$\Delta R_{c,2} = \left| \vec{AP}_c \right| - \left| \vec{A''}P_c \right| = \sqrt{(R_0 + \Delta R)^2 + X_c^2} - \sqrt{R_0^2 + (X_c - \Delta x)^2} \quad (23)$$

The slant range error of P_r is:

$$\begin{aligned}\Delta R_{r,2} &= \left| \vec{AP}_r \right| - \left| \vec{A''}P_r \right| = \sqrt{(R_0 + \Delta R)^2 + X_r^2} - \sqrt{R_0^2 + (X_r - \Delta x)^2} \\ &\approx \sqrt{(R_0 + \Delta R)^2 + \left(X_c + R_0 \cdot \frac{\theta_{BW}}{2}\right)^2} - \sqrt{R_0^2 + \left(X_c + R_0 \cdot \frac{\theta_{BW}}{2} - \Delta x\right)^2}\end{aligned}\quad (24)$$

Compared to P_c , the residual slant range error of P_r is:

$$\begin{aligned}\Delta R_{resr,2} &= \Delta R_{r,2} - \Delta R_{c,2} \\ &= \sqrt{(R_0 + \Delta R)^2 + \left(X_c + R_0 \cdot \frac{\theta_{BW}}{2}\right)^2} - \sqrt{R_0^2 + \left(X_c + R_0 \cdot \frac{\theta_{BW}}{2} - \Delta x\right)^2} \\ &\quad - \left(\sqrt{(R_0 + \Delta R)^2 + X_c^2} - \sqrt{R_0^2 + (X_c - \Delta x)^2}\right)\end{aligned}\quad (25)$$

For NB MoCo with zero-Doppler processing, the cross-point of A' on the ideal track is directly determined by the values of the platform's azimuth positions. For LOS MoCo in the 2D slant range plane, the point A'' on the ideal track is determined by the cross-point of the radar beam center line in the slant range plane (determined by LOS and the ideal track) and the ideal track fitted by the measured motion parameters.

Comparing (22) and (25), we can see that during the TOPS SAR imaging, the slant range error is varied with Δx . For further verification, we present the numerical simulation, with the parameters listed in Table 1.

Table 1. TOPS SAR slant range error simulation parameters.

Platform height	3070 m	Radar look angle	30 deg
Radar wavelength	0.03 m	Platform velocity	100 m/s
Azimuth beamwidth	3.5 deg	Pulse repetition frequency	1500 Hz
Beam-scanning angle	10 deg	Max motion displacement	0.5 m
APC distance	0.0232 m	APC array incline angle	22 deg
Bandwidth	100 MHz	Range sampling rate	125 MHz

Then, the residual phase deviations of point P_r with two different computation methods are presented in Figure 4.

From Figure 4a, we can see that the residual phase deviation is obviously azimuth-variant. However, if we consider the beam-steering direction, then the residual phase deviation across the radar beam, shown in Figure 4b, is much less than that in Figure 4a. Furthermore, the residual phase deviation is almost constant across the radar beam; therefore, the effect on SAR focusing can be ignored.

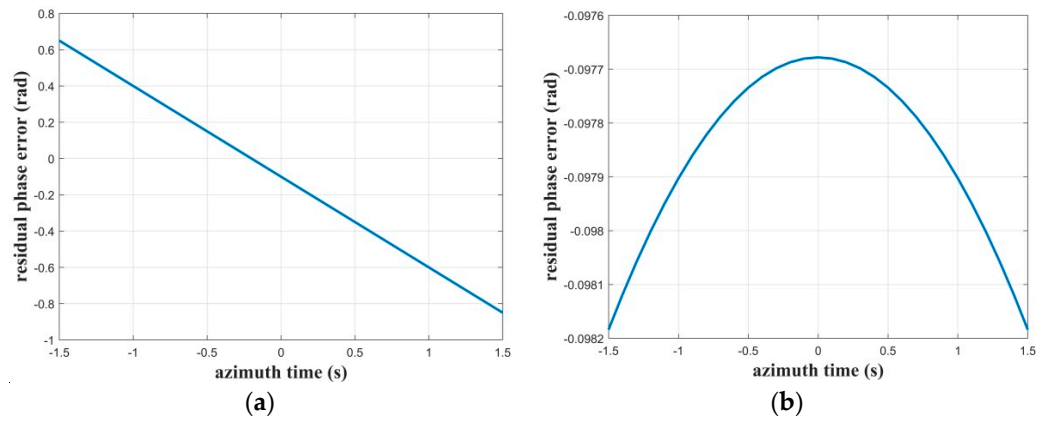


Figure 4. Residual phase deviations of P_r with two different computation methods. (a) residual phase deviation with Equation (22). (b) residual phase deviation with Equation (25).

2.2.2. Range-Dependent Radar Look Angle and Processing Strategy

Assuming that the amplitudes are the same, the received echoes of the n th channel can be expressed as (for simplicity, the azimuth time, t_m , is omitted):

$$\begin{aligned}
 s_{n,DBF}(\tau) &= w_n(\tau) \cdot s_n(\tau) \\
 &= A_0 \cdot \text{rect}\left(\frac{\tau - (\tau_1 + \Delta\tau_n)}{T}\right) \exp\left(-j2\pi f_c(\tau_1 + \Delta\tau_n) + j\pi K_r(\tau - (\tau_1 + \Delta\tau_n))^2\right) \\
 &\quad \cdot \exp\left(j\frac{2\pi}{\lambda} \cdot (n - 1)d(\sin(\theta(\tau)) - \sin \theta_0)\right)
 \end{aligned} \tag{26}$$

If $\theta(\tau)$ is small enough, then we have $\sin(\theta(\tau)) \approx \theta(\tau)$. In this case, $\theta(\tau)$ and the time delay, τ , have the linear relationship:

$$\theta(\tau) = \left. \frac{\partial\theta(\tau)}{\partial\tau} \right|_{\tau=\tau_c} (\tau - \tau_c) \tag{27}$$

where τ_c is the time delay of the scene center. However, for airborne TOPS SAR with a large-range beam, (27) will not hold.

By using the simulation parameters in Table 1, we obtained the approximation error with a large angle range of $\theta(\tau)$, which is shown in Figure 5. We can see that the larger the $\theta(\tau)$ is, the larger the approximation error is.

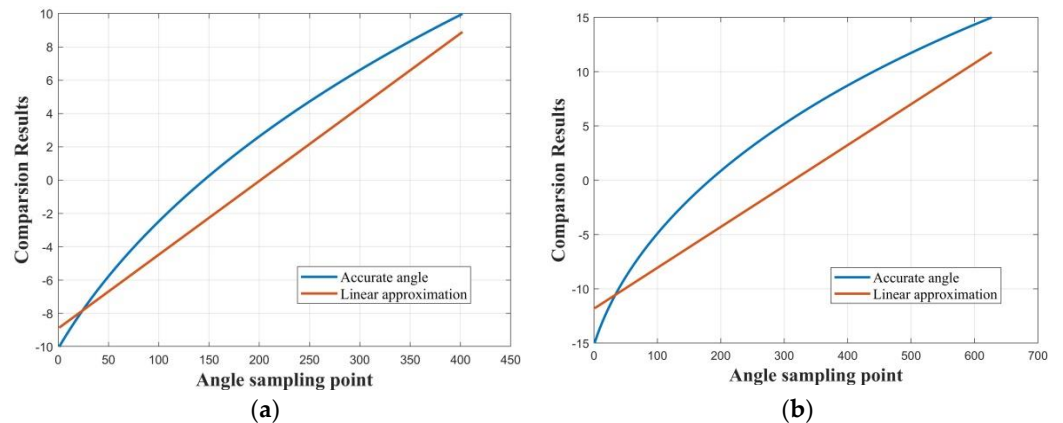


Figure 5. Linear approximation error with a large angle range of $\theta(\tau)$. (a) $\theta(\tau) \in [-10^\circ, 10^\circ]$. (b) $\theta(\tau) \in [-15^\circ, 15^\circ]$.

When (27) does not hold, the steering vector cannot be used linearly for DBF processing. Therefore, the whole range scene is divided into sub-swaths, where (27) can be held more

accurately. Each sub-swath includes m range cells. m is determined by the approximation threshold, which is defined as the approximation error $\Delta R \ll \lambda$. For the i th sub-swath, we assume $\theta(\tau) \in [\theta_{bs,i}, \theta_{be,i}]$ with $\tau_{bs,i} \leq \tau \leq \tau_{be,i}$, where $\tau_{bs,i}$ and $\tau_{be,i}$ are the time delays of the nearer start range and farther end range of the i th sub-swath, then the central time delay of the i th sub-swath is $\tau_{bc,i} = (\tau_{bs,i} + \tau_{be,i})/2$, and the DOA is $\theta_{bc,i} = (\theta_{bs,i} + \theta_{be,i})/2$. Then, the angle $\theta_{b,i}(\tau) = \theta(\tau) - \theta_{bc,i}$ of the i th sub-swath approximately meets the linear relationship:

$$\theta_{b,i}(\tau) = \left. \frac{\partial \theta_{b,i}(\tau)}{\partial \tau} \right|_{\tau=\tau_{bc,i}} \cdot (\tau - \tau_{bc,i}), \tau_{bs,i} \leq \tau \leq \tau_{be,i} \quad (28)$$

Therefore, the radar look angle in the i th sub-swath can be expressed as:

$$\theta(\tau) = \theta_{b,i}(\tau) + \theta_{bc,i}, \tau_{bs,i} \leq \tau \leq \tau_{be,i} \quad (29)$$

Then, we have:

$$\begin{aligned} \sin(\theta(\tau)) &= \sin(\theta_{b,i}(\tau) + \theta_{bc,i}) \\ &= \sin(\theta_{b,i}(\tau)) \cdot \cos(\theta_{bc,i}) + \cos(\theta_{b,i}(\tau)) \cdot \sin(\theta_{bc,i}) \end{aligned} \quad (30)$$

Due to the small value of $\theta_{b,i}(\tau)$, $\cos(\theta_{b,i}(\tau)) \approx 1$. Combining (28)–(30), we have:

$$\begin{aligned} \sin(\theta(\tau)) &\approx \sin(\theta_{b,i}(\tau)) \cdot \cos(\theta_{bc,i}) + \sin(\theta_{bc,i}) \\ &= \cos(\theta_{bc,i}) \cdot \left. \frac{\partial \theta_{b,i}(\tau)}{\partial \tau} \right|_{\tau=\tau_{bc,i}} \cdot (\tau - \tau_{bc,i}) + \sin(\theta_{bc,i}) \end{aligned} \quad (31)$$

Therefore, the radar echoes in the i th sub-swath can be expressed as:

$$\begin{aligned} s_{n,i}(\tau) &= w_n(\tau) \cdot s_n(\tau) \\ &= A_0 \cdot \text{rect}\left(\frac{\tau - (\tau_1 + \Delta\tau_n)}{T}\right) \exp\left(-j2\pi f_c(\tau_1 + \Delta\tau_n) + j\pi K_r(\tau - (\tau_1 + \Delta\tau_n))^2\right) \cdot \\ &\quad \exp\left(j\frac{2\pi}{\lambda}(n-1)d\left(\cos(\theta_{bc,i}) \cdot \left. \frac{\partial \theta_{b,i}(\tau)}{\partial \tau} \right|_{\tau=\tau_{bc,i}} (\tau - \tau_{bc,i}) + \sin(\theta_{bc,i}) - \sin\theta_0\right)\right) \end{aligned} \quad (32)$$

For simplicity, let:

$$f_0 = \frac{d}{\lambda} \cdot \cos(\theta_{bc,i}) \cdot \left. \frac{\partial \theta_{b,i}(\tau)}{\partial \tau} \right|_{\tau=\tau_{bc,i}} \quad (33)$$

$$\phi_{res} = \frac{2\pi}{\lambda} \cdot (n-1)d \left(-\cos(\theta_{bc,i}) \cdot \left. \frac{\partial \theta_{b,i}(\tau)}{\partial \tau} \right|_{\tau=\tau_{bc,i}} \cdot \tau_{bc,i} + \sin(\theta_{bc,i}) - \sin\theta_0 \right) \quad (34)$$

Substituting (33) and (34) into (32), and translating the radar echoes into the range frequency domain, we have:

$$\begin{aligned} s_{n,i}(f_r) &= G_0 \cdot \text{rect}\left(\frac{f_r - (n-1)f_0}{K_r}\right) \cdot \exp\left(-j\pi \frac{(f_r - (n-1)f_0)^2}{K_r}\right) \cdot \\ &\quad \exp(-j2\pi(f_r + f_c - (n-1)f_0) \cdot (\tau_1 + \Delta\tau_n)) \cdot \exp(j\phi_{res}) \end{aligned} \quad (35)$$

where f_r is the range frequency. From (35), we can see that the spectra of different channels are weighted by the antenna pattern in the range direction. To solve this problem, the echoes should be processed separately after weighting. When $\Delta\tau_n \cdot c < \rho_r/8$, the radar echoes $s_{n,i}(\tau)$ of the n th channel can be approximated as:

$$\begin{aligned} s_{n,i}(\tau) &\approx A_0 \cdot \text{rect}\left(\frac{\tau - \tau_1}{T}\right) \exp\left(-j2\pi f_c \tau_1 + j\pi K_r(\tau - \tau_1)^2\right) \cdot \exp(j \cdot (n-1) \cdot 2\pi f_0 \tau) \cdot \exp(j\phi_{res}) \\ &= s_{1,i}(\tau) \cdot \exp(j \cdot (n-1) \cdot 2\pi f_0 \tau) \cdot \exp(j\phi_{res}) \end{aligned} \quad (36)$$

For coherent integration of all channels, the radar echoes should be compensated to correct the phase difference between channels, and the phase compensation function $H_{n,dcom}$ is:

$$H_{n,dcom}(\tau) = \exp(-j \cdot (n - 1) \cdot 2\pi f_0 \tau) \cdot \exp(-j\phi_{res}) \quad (37)$$

Finally, the DBF-TOPS SAR result is obtained as follows:

$$s_{DBF}(\tau) = \sum_{n=1}^N s_n(\tau) \cdot H_{n,dcom}(\tau) \cdot w_n(\tau) \quad (38)$$

2.3. Channel Error Estimation and Compensation of DBF-TOPS SAR

There are two key factors of the DBF-TOPS SAR system for SAR image focusing. One is the steering vector, which is determined by the phase centers. With the known array formation and highly accurate measurement, the steering vector errors can be calibrated with high accuracy. The other factor is the difference of channels' amplitude and phase characteristics. If there are internal calibration signals, the difference of channels' amplitude and phase characteristics can be compensated easily, as is described in the Introduction Section. However, the internal calibration signals are not retained in our DBF-TOPS SAR system. Furthermore, beam-scanning of DBF-TOPS SAR with multi-channel phased array antennas may lead to changes of the channel characteristics. Therefore, the channel errors' estimation method from the radar echoes is proposed with coherence weighting, and then the relative difference of channel errors is compensated to reduce the effect on channel characteristics' changes and to improve the SNR of the DBF-TOPS SAR image.

2.3.1. Channel Error Model of DBF-TOPS SAR

In Section 2.2, the DBF-TOPS SAR was executed without channel errors. However, in the real SAR systems, the channel errors cannot be ignored. Otherwise, the coherent integration performance of DBF will be deteriorated. In this section, we will analyze the amplitude and phase errors of different channels.

In the following, the relative channel frequency response estimation from radar echoes is presented. Assuming the ideal frequency transfer function of the n th channel is $H_n^T(f_r)$, the azimuth time-dependent frequency transfer function $H_n^T(f_r, t_m)$ with channel errors can be expressed as:

$$\tilde{H}_n^T(f_r, t_m) = H_n^T(f_r) \left(1 + \Delta H_n^T(f_r, t_m)\right) \quad (39)$$

where:

$$\Delta H_n^T(f_r, t_m) \triangleq \delta_n^T(f_r, t_m) \exp\left(j\phi_n^T(f_r, t_m)\right) \quad (40)$$

In (40), $\delta_n^T(f_r, t_m)$ and $\phi_n^T(f_r, t)$ are defined as the n th channel's disturbance items of amplitude and phase, respectively. Therefore, the frequency transfer function $H_n^T(f_r, t_m)$ can be further expressed as:

$$\tilde{H}_n^T(f_r, t_m) = H_n^T(f_r) \left(1 + \delta_n^T(f_r, t_m)\right) \exp\left(j\phi_n^T(f_r, t_m)\right) \quad (41)$$

In the following, we will discuss the radar signal with channel errors. The n th channel baseband signal is shown as (8). Based on the principle of the stationary phase, the frequency domain can be expressed by:

$$S_n(f_r) = G_n \cdot \exp\left(-j\pi \frac{f_r^2}{K_r}\right) \cdot \exp\left(-j2\pi(f_c + f_r)\tau_n\right) \quad (42)$$

According to the channel error model, the n th channel radar echo in the range frequency domain with channel errors can be expressed as:

$$S_n(f_r, t_m) = G_n H(f_r) \cdot (1 + \Delta p_{e,n}(f_r, t_m)) \cdot \exp(-j\pi \frac{f_r^2}{K_r}) \cdot \exp(-j2\pi(f_c + f_r)\tau_n) \cdot \exp(j\Delta\phi_{e,n}(f_r, t_m)) + N_{e,n}(f_r, t_m) \tag{43}$$

where G_n is the window function of the n th channel in the range frequency domain, and $N_e(f_r, t_m)$ is the noise in the range frequency domain. Taking channel #1 as the referenced channel with $\Delta p_{e,1}(f_r, t_m) = 0$ and $\Delta\phi_{e,1}(f_r, t_m) = 0$, we obtain the radar signal of channel #1 as follows:

$$S_1(f_r, t_m) = G_1 H(f_r) \cdot \exp(-j\pi \frac{f_r^2}{K_r}) \cdot \exp(-j2\pi(f_c + f_r)\tau_n) + N_{e,1}(f_r, t_m) \tag{44}$$

2.3.2. Channel Error Estimation and Compensation of DBF-TOPS SAR

To estimate the channel errors, the conjugate multiplication is executed in the range frequency domain between the referenced channel and the n th channel as follows:

$$S_1(f_r, t_m) S_n^*(f_r, t_m) = G_1 G_n^* (1 + \Delta p_{e,n}(f_r, t_m)) \cdot \exp(-j\frac{2\pi}{c}(f_c + f_r)(n-1)d \cdot \sin\theta_0) \cdot \exp(-j\Delta\phi_{e,n}(f_r, t_m)) + N_{e,1,n}(f_r, t_m) \tag{45}$$

Let

$$H_r(f_r) = \exp(j2\pi/c \cdot (f_c + f_r)(n-1)d \cdot \sin\theta_0) \tag{46}$$

Compensating $H_r(f_r)$ to (45), we obtain the channel error characteristics in the range frequency domain as follows:

$$\Delta S_n(p, q) = S_1(f_r, t_m) S_n^*(f_r, t_m) H_r(f_r) \tag{47}$$

where (p, q) is the pixel location in the range frequency domain. Then, the phase of $\Delta S_n(p, q)$ is extracted to obtain the channel phase errors. However, the channel phase errors are polluted by the noise $N_{e,1,n}(f_r, t_m)$; therefore, it should be filtered to alleviate the fluctuations of the phase-frequency characteristics. In fact, the reliability of pixels is positively correlated with the channels' coherence between the reference channel and the n th channel. Therefore, we use the coherence as the weight coefficient to filter the phase-frequency response. The phase-frequency response filter is defined as:

$$H_{pha,n}(p, q) = \frac{1}{K \times L} \cdot \sum_{p=-(K-1)/2}^{(K-1)/2} \sum_{q=-(L-1)/2}^{(L-1)/2} a_n(p, q) \cdot \arg\left(\frac{\hat{S}_n(p, q)}{S_{n,sum}}\right) + \arg(S_{n,sum}) \tag{48}$$

where $a_n(p, q)$ is the normalized coherence weight, and $K \times L$ is the filter window size.

$$\begin{cases} S_{n,sum} = \sum_{p=-(K-1)/2}^{(K-1)/2} \sum_{q=-(L-1)/2}^{(L-1)/2} a_n(p, q) \cdot \hat{S}_n(p, q) \\ \hat{S}_n(p, q) = \Delta S_n(p, q) / |\Delta S_n(p, q)| \end{cases} \tag{49}$$

The coherence is estimated as follows:

$$\rho_n(p, q) = \frac{\left| \sum_{i=-(K-1)/2}^{(K-1)/2} \sum_{j=-(L-1)/2}^{(L-1)/2} S_1(p+i, q+j) \cdot S_n^*(p+i, q+j) \right|}{\sqrt{\sum_{i=-(K-1)/2}^{(K-1)/2} \sum_{j=-(L-1)/2}^{(L-1)/2} |S_1(p+i, q+j)|^2} \cdot \sqrt{\sum_{i=-(K-1)/2}^{(K-1)/2} \sum_{j=-(L-1)/2}^{(L-1)/2} |S_n(p+i, q+j)|^2}} \tag{50}$$

Then, the weight coefficient is:

$$a'_n(p, q) = \frac{\rho_n(p, q)}{\frac{1}{K \times L} \cdot \sum_{p=-(K-1)/2}^{(K-1)/2} \sum_{q=-(L-1)/2}^{(L-1)/2} \rho_n(p, q)} \quad (51)$$

Finally, the normalized weight coefficient is obtained as:

$$a_n(p, q) = \frac{a'_n(p, q)}{\max(a'_n(p, q))} \quad (52)$$

The amplitude frequency response filtering procedure is similar to the phase-frequency:

$$H_{n,amp}(p, q) = \frac{1}{K \times L} \cdot \sum_{p=-(K-1)/2}^{(K-1)/2} \sum_{q=-(L-1)/2}^{(L-1)/2} a(p, q) \cdot \frac{|S_1(f_r, t_m)|}{|S_n(f_r, t_m)|} \quad (53)$$

By using the estimated $H_{n,amp}(p, q)$ and $H_{n,pha}(p, q)$, the channel errors relative to the reference channel are calibrated. The radar echoes can be coherently integrated. Therefore, SNR will be improved as well.

2.4. Airborne DBF-TOPS SAR/InSAR Processing in Elevation

Based on the analysis in previous sections, we present the complete flowchart of airborne DBF-TOPS SAR imaging with LOS MoCo and channel equalization in Figure 6.

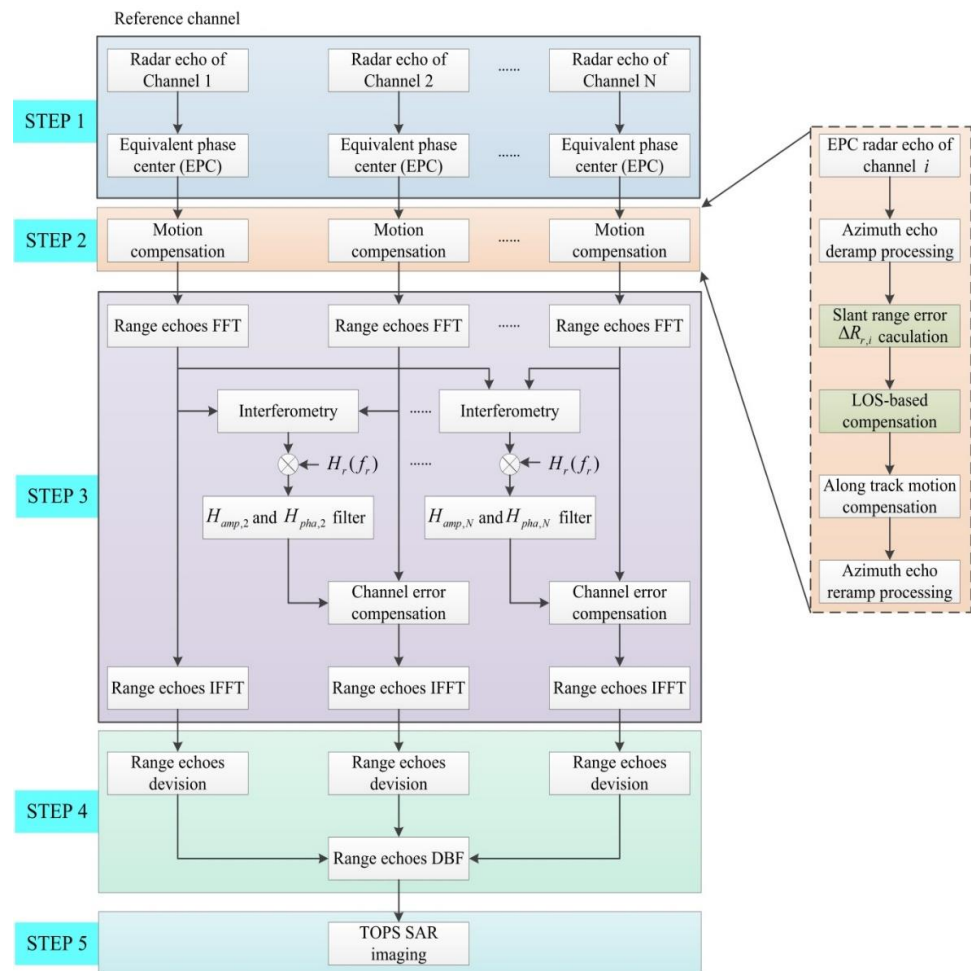


Figure 6. Flowchart of DBF-TOPS SAR imaging with LOS MoCo and channel equalization.

The airborne DBF-TOPS SAR imaging method mainly includes five steps.

STEP 1. Multi-channel TOPS SAR echoes achievement with EPC principle.

There are four reception channels in the DBF-TOPS SAR system in this paper. The multi-channels of DBF-TOPS SAR in elevation work with single-channel transmission and four-channel reception. Therefore, with the EPC principle, the radar positions of transmission are the same as those of reception during the pulse-repetition time. The phase compensation (calculated by the time delay) procedure of EPC is shown in Section 2.1.

STEP 2. LOS MoCo of single-channel TOPS SAR data is executed with all channels in elevation.

With the motion parameters and posture parameters obtained from the measurement instrument and the relative position relationships of the multi-channels, the range displacement of each channel (after EPC equivalence) is calculated and compensated one-by-one.

The detailed procedure is given below:

- (i). With the measured motion and posture parameters, the phase center's position of each channel can be directly calculated.
- (ii). The ideal flight path of the referenced channel is linearly fitted by the phase center's position.
- (iii). The other three channels' ideal flight paths are obtained by the translation of the ideal flight path of the referenced channel with the tilt angle of the linear array antennas.
- (iv). The range displacement of each channel is calculated and compensated. Then, the compensation in the range direction is completed.
- (v). For azimuth compensation, the main procedure is to interpolate the nonuniform sampling positions, caused by the forward speed of the platform, to uniform sampling positions, which is similar to [45,47]. The procedure of the LOS motion displacement calculation is shown in Section 2.2.1.

STEP 3. Channel amplitude error and phase error relative to the referenced channel are estimated by using the coherence weighted filter.

After motion compensation, the range displacement and imaging geometric model mismatch are calibrated. However, the transfer function of each elevation channel is different because of the non-ideal electrical characteristics and the non-ideal manufacturing factors. Therefore, the transfer functions should be estimated and calibrated between channels.

The detailed estimation and compensation of channel amplitude error and phase error can be found in Section 2.3. It should be noted that the amplitude error and phase error are compensated by taking channel #1 as a reference. The main purpose of the procedure is to eliminate the differences of transfer functions between channels.

If we have the inner calibration signals of each channel, the channel errors can be directly compensated by the inner calibration signals.

The channel errors' estimation is shown in Section 2.3.

STEP 4. To overcome the approximation error with a large range of $\theta(\tau)$, the range echoes are divided into sub-swaths for DBF in elevation.

After motion compensation and channel characteristics' calibration to the referenced channel, DBF can be executed with sub-swaths' division by using the method in Section 2.2.2.

STEP 5. The conventional TOPS SAR focusing method is used to obtain the final TOPS SAR image.

After DBF processing, the radar echoes are coherently integrated in elevation. Therefore, the single-channel TOPS SAR method [15,16,45] can be used to formulate the focused image.

3. DBF-TOPS SAR/InSAR Experiment Results

3.1. SAR Imaging Simulation Results

By using the simulation parameters in Table 1, we will quantitatively investigate the TOPS SAR imaging performance. The motion displacements in the Cartesian coordinate system are presented in Figure 7.

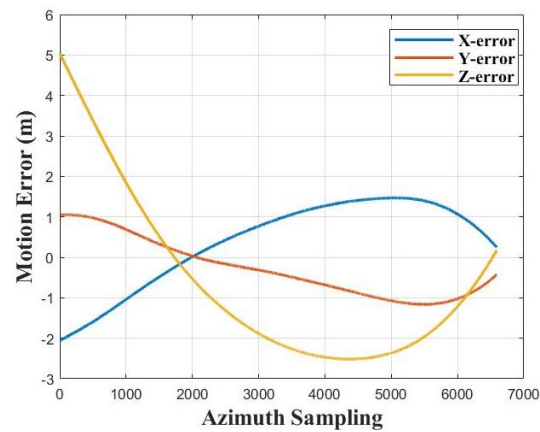


Figure 7. Motion displacements in the Cartesian coordinate system.

We set 3×3 points in the scene. The point target responses with different MoCo methods are shown in Figure 8. Among these results, Figure 8a–c are the point target responses without MoCo, Figure 8e–f are the point target responses with NB MoCo, and Figure 8g–i are the point target responses with LOS MoCo. The second and third columns of Figure 8 show us the enlarged area of the first column, which is more convenient to show the point focusing performance at the beam edge. From Figure 8, we can see that the focusing performance of LOS MoCo is better than that of NB MoCo.

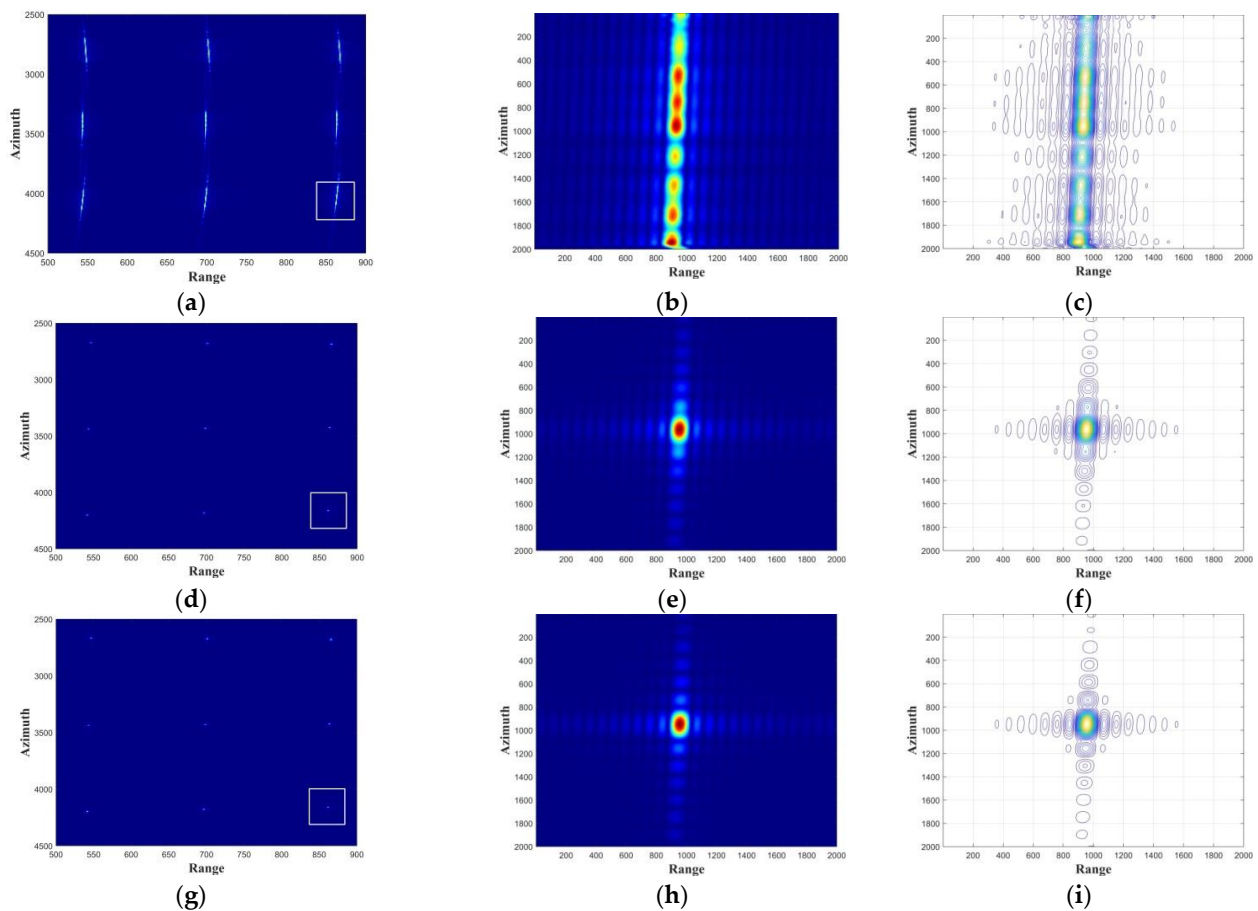


Figure 8. Simulation results with different MoCo methods. (a) 3×3 point targets without MoCo. (b) Enlarged rectangle area of (a). (c) Slice of (b). (d) 3×3 point targets with NB MoCo. (e) Enlarged rectangle area of (d). (f) Slice of (e). (g) 3×3 point targets with LOS MoCo. (h) Enlarged rectangle area of (g). (i) Slice of (h).

For further comparison, the performance of different MoCo methods with quantitative values is shown in Table 2. The principal phase values in the main lobe are also presented. PS LR means the peak sidelobe ratio. IS LR means the integral sidelobe ratio.

Table 2. Quantitative performance comparison of points in the rectangle.

	Without MoCo	NB MoCo	LOS MoCo
Range PS LR (dB)	−13.2896	−13.2042	−13.2961
Range IS LR (dB)	−10.1264	−10.0880	−10.2144
Azimuth PS LR (dB)	−1.1598	−10.0973	−13.2765
Azimuth IS LR (dB)	4.6288	−7.3650	−10.0711
Range resolution (m)	1.6641	1.6642	1.6641
Azimuth resolution (m)	—	4.6728	4.4682
Phase error (rad)	—	−0.7836	−0.5036

From the processing results of Figure 8 and Table 2, we can see that the focusing results of LOS MoCo are better than those of NB MoCo. The ideal principal phase value of the point in the rectangle is -0.4988 rad. For the phase preservation performance evaluation, the absolute phase error of NB MoCo is 0.2824 rad, compared to 0.0048 rad of LOS MoCo. From the residual phase error, we can see that LOS MoCo is better for InSAR processing than NB MoCo. Assuming the InSAR baseline length is 0.4 m, and the baseline tilt angle is 0 deg, the ambiguity height of InSAR with the parameters in Table 1 is 134.98 m. Therefore, the relative DEM height errors induced by MoCo residual phase errors are 8.5796 m of NB MoCo and 0.1458 m of LOS MoCo, respectively, which shows the effectiveness for LOS MoCo on the phase preservation performance.

3.2. Real Data Results of DBF-TOPS SAR in Elevation

In this section, the real DBF-TOPS SAR/InSAR experimental data acquired in Guangdong Province, China, in September (2019) are used for performance investigation. We first investigate the processing results of single-channel TOPS SAR imaging and then the DBF-TOPS SAR radar echoes are processed. Furthermore, we will use the DEM generation accuracy of DBF-TOPS InSAR for phase reservation evaluation. The real SAR data parameters are shown in Table 3.

Table 3. Parameters of airborne DBF-TOPS SAR in elevation.

Nearest slant range	2553 m	Radar range beam	20–40 deg
Radar center frequency	35.7 GHz	Mean platform velocity	36 m/s
Azimuth beamwidth	0.96 deg	Pulse-repetition frequency	1500 Hz
Beam-scanning angle	5.2 deg	Beam-steering velocity	1.404 deg/s
APC distance (EPCs)	0.0132 m	Bandwidth	100 MHz
Range sampling rate	125 MHz	InSAR baseline tilt angle	0 deg
InSAR baseline	0.4 m	Channel number	4

The DBF-TOPS SAR is composed of four channels after EPC processing. For the combination of DBF and TOPS SAR, all DBF channels operate the same steering vector for TOPS SAR with phased array antennas, simultaneously. The channels' range beams cover the full swath (20–40 degrees incidence) at the same time, and the channels receive ground echoes simultaneously during the pulse-repetition time. Then, the radar echoes based on LOS MoCo are relatively calibrated with channel error estimation and compensation to improve the SNR of the DBF-TOPS SAR image.

3.2.1. Single-Channel TOPS SAR MoCo Investigation

The radar beam in the range is 20 degrees (from 20 to 40 deg), and the linear approximation relationship does not hold, as discussed in Section 2.2.2. Therefore, the range swath should be divided into sub-swaths. The imaging results of a single burst are shown in Figure 9. Figure 9a is the result with NB MoCo, and Figure 9b is the result with LOS MoCo. For clarity, we select the corner reflector in the scene to evaluate the focusing results, shown in Figure 10. There are three corner reflectors in the scene, and the corner reflectors are marked in Figure 9b with white circles.

Comparing the profiles of the corner reflector CR#1, we can see that the profiles of LOS MoCo are better than those of the NB MoCo. The main lobe in azimuth of LOS MoCo is obviously narrower than that of NB MoCo. However, the phase preservation performance cannot be directly evaluated from the corner reflectors, which will be further evaluated from the generated DEM with TOPS InSAR. The focusing performance comparison is shown in Table 4.

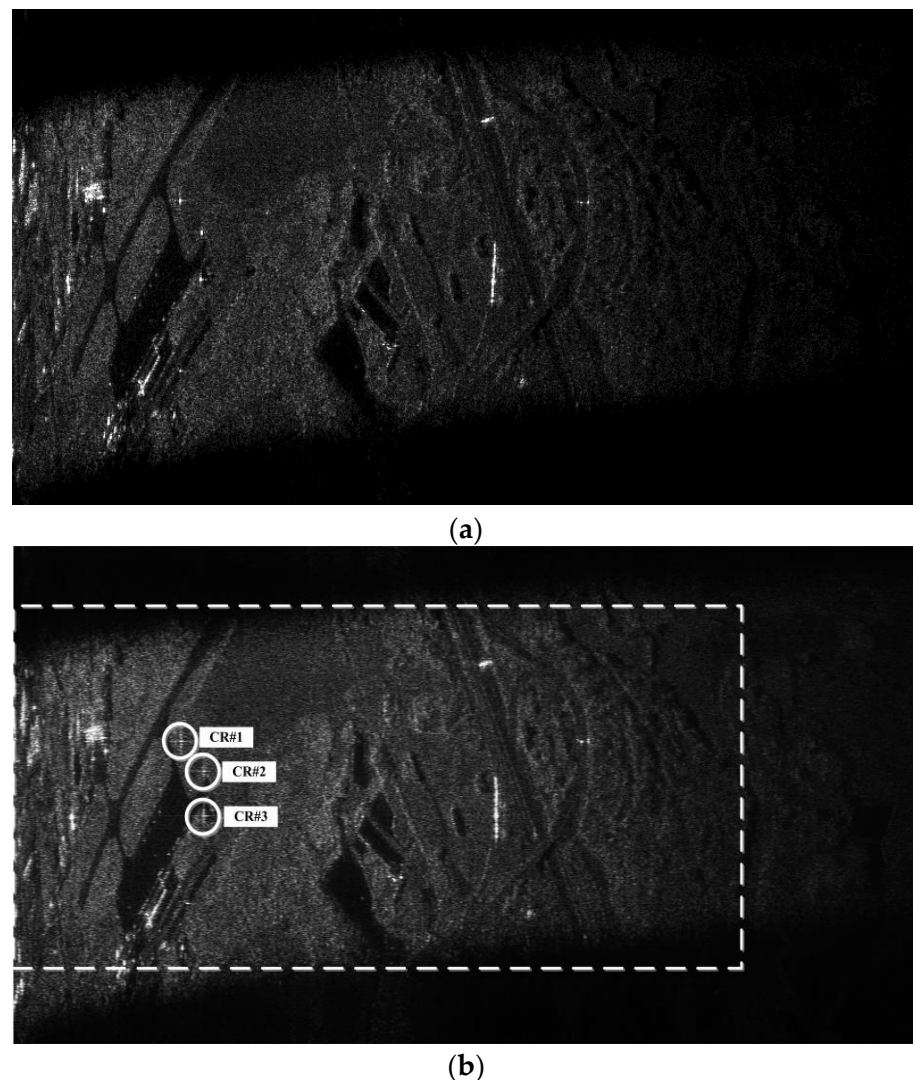


Figure 9. One-burst imaging results of single-channel TOPS SAR. (a) Imaging result with NB MoCo. (b) Imaging result with LOS MoCo.

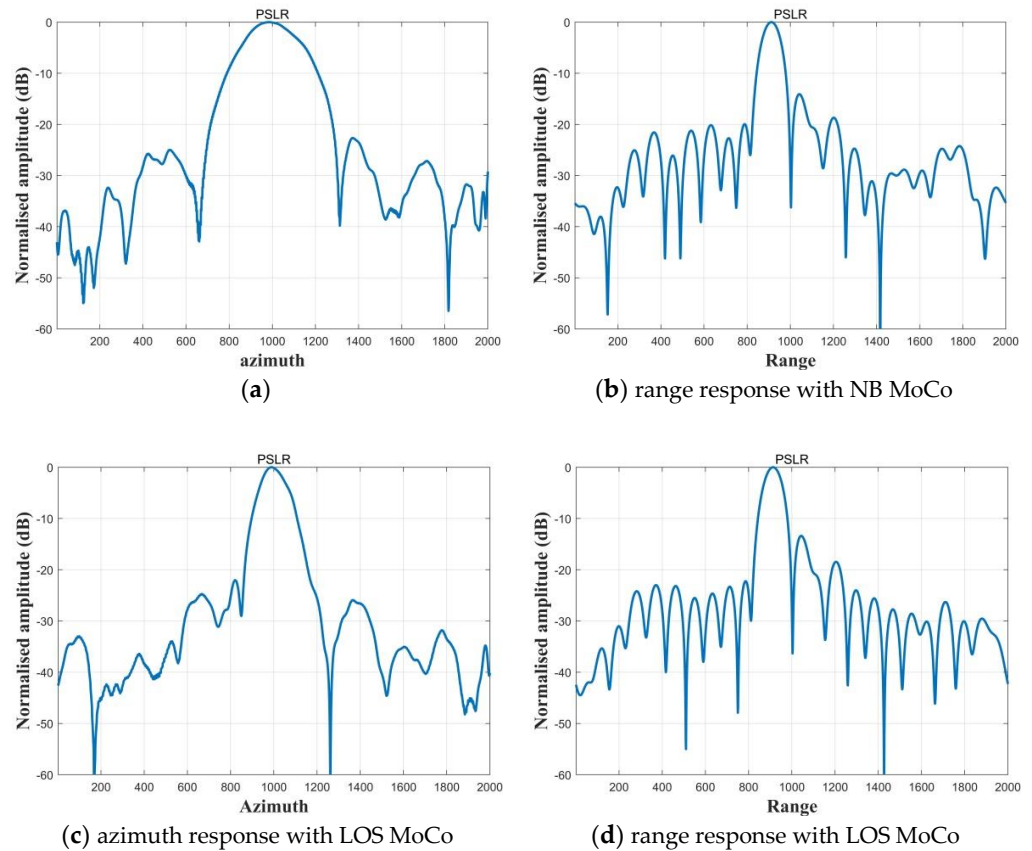


Figure 10. Corner reflector profiles of CR#1 with different MoCo methods. (a) Azimuth response with NB MoCo. (b) Range response with NB MoCo. (c) Azimuth response with LOS MoCo. (d) Range response with LOS MoCo.

Table 4. Evaluation of corner reflectors of CR#1.

	Azimuth PSLR (dB)	Range PSLR (dB)	Azimuth ISLR (dB)	Range ISLR (dB)	Azimuth Resolution (m)	Range Resolution (m)
NB MoCo	−16.9323	−14.0987	−21.4223	−11.3375	1.1244	1.4570
LOS MoCo	−22.2106	−13.4000	−20.2500	−11.7600	0.7244	1.4930

From Table 4, we can see that the azimuth focusing performance is obviously improved with LOS MoCo, with 0.6025 m, compared to the NB MoCo of 1.3426 m.

3.2.2. DBF-TOPS SAR Imaging in Elevation

In this section, we use the four-channel (after EPC processing) DBF-TOPS SAR system to investigate the focusing performance of DBF in elevation. Channel #1 is taken as the reference channel. Before TOPS SAR focusing, the echoes of each channel are compensated with a phase term by using EPC equivalence. Furthermore, the two sets of four-channel antennas are formulated in the DBF-TOPS SAR system. Therefore, InSAR DEM generation can be executed after focusing, as shown in the next section.

In the following, we will investigate the channel errors' characteristics. Taking channel #2 as an example, Figure 11 shows us the channel errors between channels #2 and #1. Figure 11a shows the channel phase error of channel #2 relative to channel #1. Figure 11b shows the channel phase error after compensation, which shows us the zero-round distribution phase error after compensation in the range frequency domain. Figure 11c shows the channel amplitude imbalance of channel #2 relative to channel #1, and we can see that the amplitude ratio varies along the range direction. After channel amplitude imbalance

compensation, the amplitude ratio equals almost 1 in the range frequency domain, as is shown in Figure 11d.

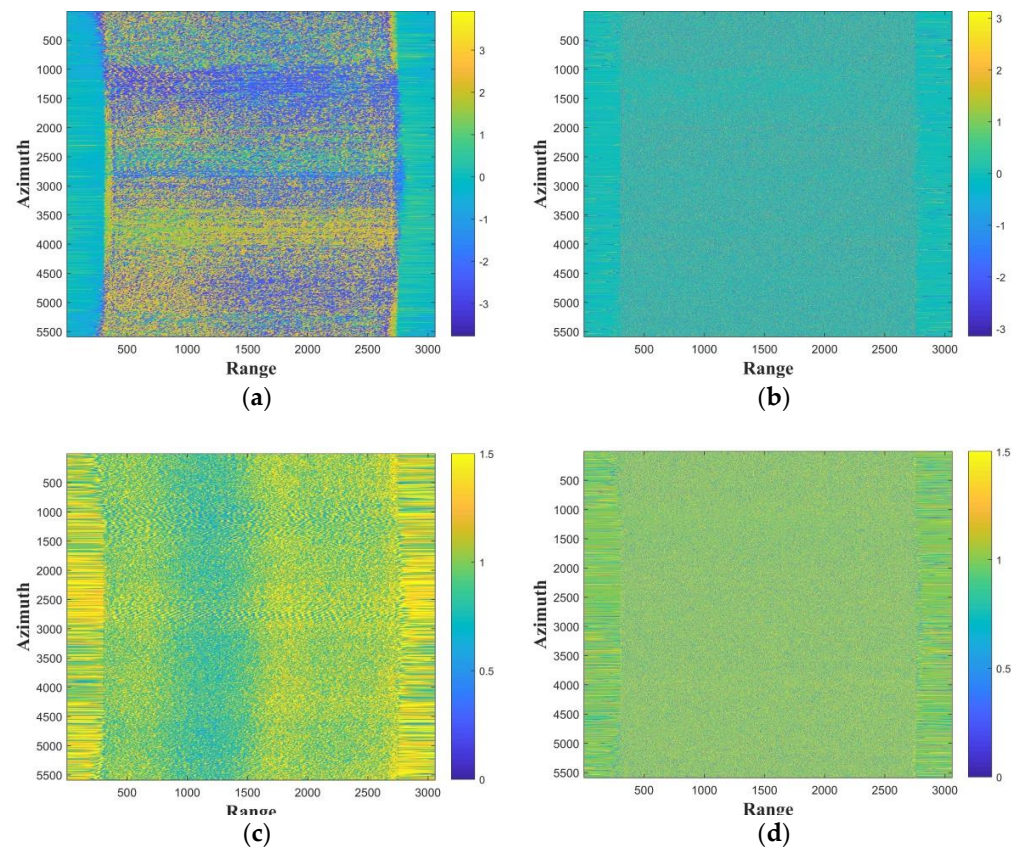


Figure 11. Channel errors' characteristics and compensation results. (a) Phase error between channels #1 and #2. (b) Phase error after compensation. (c) Amplitude ratio of channel #2 relative to #1. (d) Amplitude ratio after calibration.

In the following, we will further analyze the channel coherence without/with channel errors' compensation. Figure 12 shows the coherence histograms without/with channel errors' compensation between channels #1 and #2. We can see that the coherence is improved with channel errors' compensation, and the mean value is larger than that without channel errors' compensation.

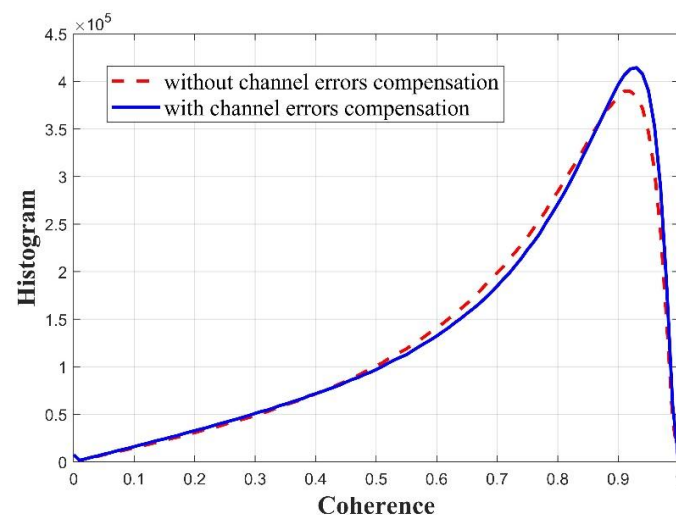


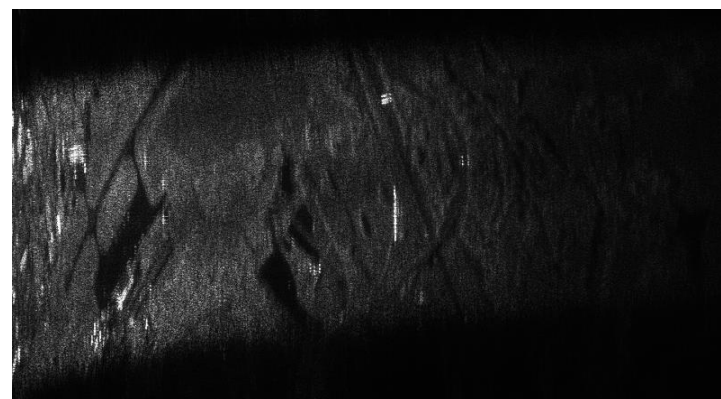
Figure 12. Coherence histograms without/with channel errors' compensation.

Furthermore, we present the coherence mean values between channels in Table 5. From Table 5, we can see that the coherences with channel errors' compensation are better than those without channel errors' compensation. Since the characteristics of each channel are not the same as each other, the coherence improvement is also different between channel pairs.

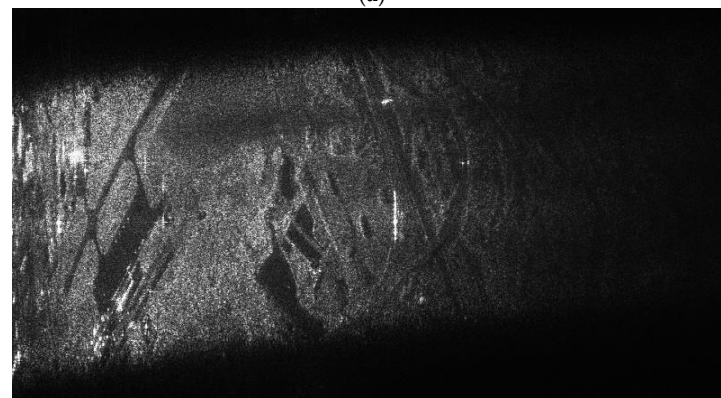
Table 5. Mean coherence values of different channel pairs.

	Channels #1 and #2	Channels #1 and #3	Channels #1 and #4
Mean coherence values without channel errors' compensation	0.6791	0.6909	0.6689
Mean coherence values with channel errors' compensation	0.7508	0.7461	0.7617

With the channel error-compensated radar echoes, we execute the DBF processing for the TOPS SAR in elevation. The DBF-TOPS SAR imaging result without channel errors' compensation is shown in Figure 13a, and the channel error-compensated DBF-TOPS SAR focusing result is shown in Figure 13b. The DBF results are based on LOS MoCo of the single channel. The quantization bits are the same for Figure 13a,b. We can see that the power of Figure 13b is obviously larger than that of Figure 13a, which shows the effect of coherent integration after channel errors' compensation. Furthermore, the DBF-TOPS SAR image of Figure 13a without channel errors' compensation has ambiguity in the azimuth direction compared to Figure 13b.



(a)



(b)

Figure 13. Focusing results of DBF-TOPS SAR in elevation. (a) DBF-TOPS SAR result without channel errors' compensation. (b) DBF-TOPS SAR result with channel errors' compensation.

With the focused TOPS SAR images, Table 6 shows us the SNR comparison of DBF.

Table 6. SNR comparison.

	Single-Channel Image	DBF without Channel Errors' Compensation	DBF with Channel Errors' Compensation
SNR (dB)	11.24	12.56	16.33

From Table 6, we can see that the SAR image's SNR of DBF is improved by 5.09 dB compared to the single-channel image, which shows us the effectiveness of the DBF with channel errors' compensation.

3.3. DBF-TOPS InSAR Experiment

In this section, we present the TOPS InSAR processing results with different experiment conditions. For the low SNR of images in the far range (right part of the images) with large incidence angles, we select the areas in the white rectangle shown in Figure 9b to perform InSAR processing. We provide three cases for performance comparison. The first case is based on the NB MoCo method, the second case is based on the LOS MoCo, and the third case is obtained by LOS MoCo-based DBF in elevation. The interferometric fringes are shown Figure 14a–c, and the DEMs are shown in Figure 14d–f. The phase preservation performance is different for the three given cases. Therefore, the interferometric fringes' distribution is different, which leads to the DEM generation accuracy difference.

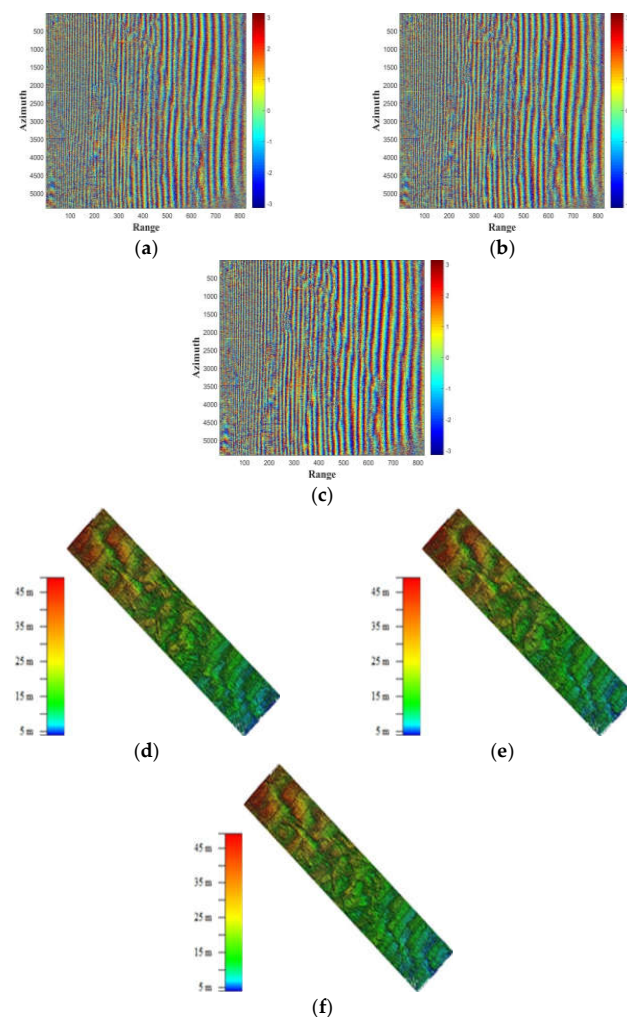


Figure 14. InSAR fringes and DEMs with different processing strategies. (a) NB MoCo-based fringe. (b) LOS MoCo-based fringe. (c) LOS MoCo-based DBF fringe. (d) NB MoCo-based DEM. (e) LOS MoCo-based DEM. (f) LOS MoCo-based DBF DEM.

To evaluate the DEM accuracy of Figure 14, we evaluate the height values of the corner reflectors shown in Figure 9b. The results are shown in Table 7.

Table 7. DEM height evaluation of corner reflectors.

	CR#1	CR#2	CR#3	Relative Height Accuracy
DEM height (m)	7.1380	7.9020	7.1790	0.6078
NB MoCo-based DEM	8.4436	5.4392	−12.3744	15.9137
LOS MoCo-based DEM	10.5928	13.1699	6.4729	4.7772
LOS MoCo-based DBF DEM	8.6246	8.5726	10.4143	1.4830

From the generated InSAR DEM, we can see that the relative height of the corner reflectors of NB MoCo-based DEM is larger than that of the LOS MoCo-based DEM, and this is because the LOS MoCo method has better phase preservation performance. The relative height of LOS MoCo-based DEM is larger than that of LOS MoCo-based DBF DEM, and the reason is that the InSAR image pairs have higher SNR with DBF than the single-channel image pairs. That is to say, the coherence of DBF-TOPS InSAR is larger than the single-channel TOPS InSAR. The improved SNR and high coherence of SAR images lead to small InSAR phase fluctuation. Therefore, the relative height accuracy of DEM is improved.

4. Discussion

The challenge of the investigated SAR system is embodied in two aspects. The first aspect is the motion compensation for phase preservation with a wide beam angle and squint angle. Motion compensation is necessary for SAR and InSAR imaging. There are extensive MoCo methods for different SAR imaging modes, including TOPS SAR. MoCo methods are mainly divided into two categories. One is based on high-accuracy measuring instruments, such as IMU. The other is based on the motion parameters' estimation from data, such as the map drift method and PGA. However, most of these methods show the focused SAR images without phase preservation performance investigation, which is very important for the applications, such as InSAR, GMTI, etc.

Some echo data-based methods estimate phase errors without considering the radar geometric relationship of radar data acquisition, such as PGA. Intrinsically, coherent integration is in-phase addition of the radar signals. Therefore, all the phases should be calibrated to a referenced phase for coherent integration. If the referenced phase is not the phase corresponding to the 2π module of the slant range, then the principal phase value in the focused main lobe is not equal to the 2π module of the slant range, though the focused point target envelope is still correct.

Herein, we have provided a numerical example to explain the importance of phase preservation. Generally, the phase history/slant range history is assumed to be a hyperbolic curve. If the principal phase value is zero (2π module of slant range), then the coherent integration can be successfully executed with other phase values calibrated to zero. The principal phase value in the focused main lobe is zero. However, if we select another reference phase value, such as $\pi/4$, on the hyperbolic curve, then the phase values should be calibrated to $\pi/4$ for coherent integration. In this case, the focused envelope is still correct. However, the phase value in the main lobe will be $\pi/4$, which is quite different from the principal phase value of zero (2π module of slant range). The biased phase value will have a great effect on InSAR processing because the phase value and the InSAR geometry are mismatched.

For phase preservation, the motion displacement is often calculated from the high-accuracy measuring instrument rather than from echo data-based methods. Therefore, the InSAR systems often complete MoCo with a high-accuracy measuring instrument to maintain the radar echoes' acquisition geometry, as was discussed in this paper.

The second aspect of the investigated DBF-TOPS SAR system in elevation is channel errors' calibration and DBF with a large angle range. Since the channel errors are not related to the radar imaging geometry, then the channel errors can be estimated from radar echoes. If the internal calibration signals of the channels are given, then the channel errors can be easily calibrated. For DBF with a large angle range, the approximation criterion was discussed. From the experimental results, the effectiveness was also validated. However, the sub-swaths' division may lead to an image mosaicking problem, which was solved here by the range echoes overlapping between adjacent sub-swaths. From the InSAR fringes and DEMs, we can see that image mosaicking caused by sub-swaths had almost no effect on the InSAR results.

In the future, the more accurate and high-efficiency processing method for DBF-TOPS SAR in elevation with a wide beam angle and squint angle should be further investigated. The processing flowchart in the paper provides some inspiration for the new system of DBF-TOPS SAR, which combines the advantages of DBF for SNR improvement and TOPS SAR for the wide scene coverage.

5. Conclusions

In this paper, we investigated the processing flowchart of DBF-TOPS SAR in elevation considering the phase preservation, which is the key factor for DBF-TOPS InSAR DEM generation. Based on the imaging model and the analysis of motion displacement, the residual phase deviation variation characteristics in azimuth with squint angle were investigated in detail. For the InSAR demand of phase preservation, the airborne TOPS SAR motion compensation method was presented along the LOS direction. Compared to the NB MoCo, the phase residual deviation of LOS MoCo was greatly decreased, and the variance of the phase residual error was also obviously reduced, which validates the effectiveness of LOS MoCo. For the large beam angle range, the range-dependent steering vector of DBF was executed with sub-swaths' division. Then, the channel errors' estimation and compensation method with coherence weighting in the frequency domain was presented for DBF in elevation. To evaluate the phase preservation performance, DBF-TOPS InSAR data were processed for DEM generation, and the generated DEMs under different experimental conditions were compared. Among those DEM results, the relative height accuracy of LOS MoCo-based DEM was better than NB MoCo-based DEM, because there was less residual phase error with LOS MoCo. The LOS MoCo-based DBF showed the best accuracy of those results because of the improved SNR by DBF and less residual phase error with LOS MoCo. Through the processing results of simulated data and real airborne DBF-TOPS SAR/InSAR data, the effectiveness of the proposed flowchart was validated.

Author Contributions: Conceptualization, Z.S. and H.X.; methodology, Z.S.; software, J.T., H.X., L.Z. and C.X.; validation, Z.S. and C.X.; formal analysis, Z.S. and H.X.; investigation, Z.S. and J.T.; resources, Z.S.; data curation, Z.S. and T.W.; writing—original draft preparation, Z.S., J.T., H.X. and L.Z.; writing—review and editing, Z.S. and H.X.; visualization, Z.S.; supervision, Z.S.; project administration, Z.S.; funding acquisition, T.W. All authors have read and agreed to the published version of the manuscript.

Funding: This research was funded by the National Natural Science Foundation of China under grant number 61671355.

Data Availability Statement: Not applicable.

Conflicts of Interest: The authors declare no conflict of interest.

References

1. Currie, A.; Brown, M.A. Wide swath SAR. *IEEE Proc. F* **1992**, *139*, 122–135. [[CrossRef](#)]
2. Krieger, G.; Gebert, N.; Moreira, A. Unambiguous SAR signal reconstruction from nonuniform displaced phase center sampling. *IEEE Geosci. Remote Sens. Lett.* **2004**, *1*, 260–264. [[CrossRef](#)]
3. Li, Z.; Wang, H.; Su, T.; Bao, Z. Generation of wide-swath and high-resolution SAR images from multichannel small spaceborne SAR systems. *IEEE Geosci. Remote Sens. Lett.* **2005**, *2*, 82–86. [[CrossRef](#)]

4. Krieger, G.; Gebert, N.; Moreira, A. Multidimensional waveform encoding: A new digital beamforming technique for synthetic aperture radar remote sensing. *IEEE Trans. Geosci. Remote Sens.* **2008**, *46*, 31–46. [[CrossRef](#)]
5. Bamler, R.; Eineder, M. ScanSAR processing using standard high precision SAR algorithms. *IEEE Trans. Geosci. Remote Sens.* **1996**, *34*, 212–218. [[CrossRef](#)]
6. Zan, F.D.; Guarnieri, A.M. TOPSAR: Terrain observation by progressive scans. *IEEE Trans. Geosci. Remote Sens.* **2006**, *44*, 2352–2360. [[CrossRef](#)]
7. Prats, P.; Scheiber, R.; Mittermayer, J.; Meta, A.; Moreira, A. Processing of sliding spotlight and TOPS SAR data using baseband azimuth scaling. *IEEE Trans. Geosci. Remote Sens.* **2010**, *48*, 770–780. [[CrossRef](#)]
8. Suo, Z.; Li, Z.; Bao, Z. Multi-channel SAR-GMTI method robust to coregistration error of SAR images. *IEEE Trans. Aerosp. Electron. Syst.* **2010**, *46*, 2035–2043. [[CrossRef](#)]
9. Chen, S.; Wang, H.; Xu, F.; Jin, Y.-Q. Target classification using the deep convolutional networks for SAR images. *IEEE Trans. Geosci. Remote Sens.* **2016**, *54*, 770–780. [[CrossRef](#)]
10. Cao, N.; Lee, H.; Zaugg, E.; Shrestha, R.; Carter, W.E.; Glennie, C.; Lu, Z.; Yu, H. Estimation of residual motion errors in airborne SAR interferometry based on time-domain backprojection and multisquint techniques. *IEEE Trans. Geosci. Remote Sens.* **2018**, *56*, 2397–2406. [[CrossRef](#)]
11. Meta, A.; Prats, P.; Steinbrecher, U.; Mittermayer, J.; Scheiber, R. First TOPSAR image and interferometry results with TerraSAR-X. In Proceedings of the Fringe Workshop, Noordwijk, The Netherlands, 23–25 April 2008; European Space Agency: Noordwijk, The Netherlands, 2008; pp. 1–8.
12. Prats, P.; Scheiber, R.; Marotti, L.; Wollstadt, S.; Reigber, A. TOPS interferometry with TerraSAR-X. *IEEE Trans. Geosci. Remote Sens.* **2012**, *50*, 3179–3188. [[CrossRef](#)]
13. Sentinel 1. Available online: <https://sentinel.esa.int/web/sentinel/missions/sentinel-1>. (accessed on 6 August 2022).
14. Li, Z.; Wang, H.; Bao, Z.; Wang, H.; Liao, G. Performance improvement for constellation SAR using signal processing techniques. *IEEE Trans. Aerosp. Electron. Syst.* **2006**, *42*, 436–452.
15. Engen, G.; Larsen, Y. Efficient full aperture processing of TOPS Mode data using the moving band chirp Z-transform. *IEEE Trans. Geosci. Remote Sens.* **2011**, *49*, 3688–3693. [[CrossRef](#)]
16. Sun, G.; Xing, M.; Wang, Y.; Wu, Y.; Wu, Y.; Bao, Z. Sliding spotlight and TOPS SAR data processing without subaperture. *IEEE Geosci. Remote Sens. Lett.* **2011**, *8*, 1036–1040. [[CrossRef](#)]
17. Rodon, J.R.; Broquetas, A.; Arbecu, J.M.G.; Closa, G.; Labriola, M. Signal-to-noise ratio equalization for TOPSAR mode using a nonuniform steering rate. *IEEE Geosci. Remote Sens. Lett.* **2012**, *9*, 199–203. [[CrossRef](#)]
18. Fan, H.; Zhang, Z.; Wang, R.; Li, N.; Xu, W.; Xu, Z. Demonstration of dual-channel TOPS SAR imaging with airborne C-band data. *IEEE J. Sel. Top. Appl. Earth Observ. Remote Sens.* **2017**, *10*, 3569–3581. [[CrossRef](#)]
19. Li, N.; Wang, R.; Deng, Y.; Zhao, T.; Wang, W.; Zhang, H. Processing sliding mosaic mode data with modified full-aperture imaging algorithm integrating scalloping correction. *IEEE J. Sel. Top. Appl. Earth Observ. Remote Sens.* **2017**, *10*, 1804–1812. [[CrossRef](#)]
20. Guan, Y.; Chang, W. Study on full aperture imaging algorithm for airborne TOPS mode. *IEEE Access* **2018**, *6*, 16305–16313. [[CrossRef](#)]
21. Wang, J.; Liang, X.; Chen, L.; Li, Y. First demonstration of airborne MIMO SAR system for multimodal operation. *IEEE Trans. Geosci. Remote Sens.* **2022**, *60*, 5204113. [[CrossRef](#)]
22. Manzoni, M.; Rizzi, M.; Tebaldini, S.; Monti-Guarnieri, A.V.; Prati, C.M.; Tagliaferri, D.; Nicoli, M.; Russo, I.; Mazzucò, C.; Duque, S.; et al. Residual motion compensation in automotive MIMO SAR imaging. In Proceedings of the 2022 IEEE Radar Conference (RadarConf22), New York, NY, USA, 21–25 March 2022; pp. 1–7.
23. Liu, Y.; Wang, H.; Yu, W. The study on adaptive digital beam-forming algorithms on elevation for Ka-band spaceborne SAR. *J. Signal Process.* **2015**, *31*, 808–814.
24. Rincon, R.F.; Vega, M.A.; Buefil, M.; Geist, A.; Hilliard, L.; Racette, P. DBSAR's first multimode flight campaign. In Proceedings of the 8th European Conference on Synthetic Aperture Radar, EUSAR 2010, Aachen, Germany, 7–10 June 2010; pp. 1178–1181.
25. Rincon, R.F.; Vega, M.A.; Buefil, M.; Geist, A.; Hilliard, L.; Racette, P. NASA's L-band digital beamforming synthetic aperture radar. *IEEE Trans. Geosci. Remote Sens.* **2011**, *49*, 3622–3628. [[CrossRef](#)]
26. Rincon, R.; Fatoyinbo, T.; Osmanoglu, B.; Lee, S.-K.; Ranson, K.J.; Marrero, V.; Yearly, M. Development of NASA's next generation L-band digital beamforming synthetic aperture radar (DBSAR-2). In Proceedings of the EUSAR 2016: 11th European Conference on Synthetic Aperture Radar, EUSAR 2016, Hamburg, Germany, 6–9 June 2016; pp. 1251–1254.
27. Bertl, S.; Lopez-Dekker, P.; Wollstadt, S.; Krieger, G. Demonstration of digital beamforming in elevation for spaceborne synthetic aperture radar. *EUSAR 2014, 2014*, 205–208.
28. Wang, W.; Wang, R.; Deng, Y.; Hou, L.; Xu, W.; Guo, L. A processing scheme for LFM-based waveform MIMO SAR with digital beam-forming in elevation. *Remote Sens. Lett.* **2015**, *6*, 874–883. [[CrossRef](#)]
29. Wang, R.; Wang, W.; Shao, Y.; Hong, F.; Wang, P.; Deng, Y.; Zhang, Z.; Loffeld, O. First bistatic demonstration of digital beamforming in elevation with terra SAR-X as an illuminator. *IEEE Trans. Geosci. Remote Sens.* **2016**, *54*, 842–849. [[CrossRef](#)]
30. Yang, T.; Wang, Y.; Chen, G. Digital beamforming in elevation for spaceborne HRWS SAR based on sparse DOA estimation. *Remote Sens. Lett.* **2017**, *8*, 448–457. [[CrossRef](#)]

31. Yang, T.; Lv, X.; Wang, Y.; Qian, J. Study on a novel multiple elevation beam technique for HRWS SAR system. *IEEE J. Sel. Top. Appl. Earth Observ. Remote Sens.* **2015**, *8*, 5030–5039. [[CrossRef](#)]
32. Chen, Z.; Zhang, Z.; Qiu, J.; Zhou, Y.; Wang, W.; Fan, H.; Wang, R. A novel motion compensation scheme for 2-D multichannel SAR systems with quaternion posture calculation. *IEEE Trans. Geosci. Remote Sens.* **2021**, *59*, 9350–9360. [[CrossRef](#)]
33. Villano, M.; Peixoto, M.N. Characterization of nadir echoes in multiple elevation-beam SAR with constant and variable pulse repetition interval. *IEEE Trans. Geosci. Remote Sens.* **2022**, *60*, 5215609. [[CrossRef](#)]
34. Zhou, Y.; Wang, W.; Chen, Z.; Wang, P.; Zhang, H.; Qiu, J.; Zhao, Q.; Deng, Y.; Zhang, Z.; Yu, W.; et al. Digital beamforming synthetic aperture radar (DBSAR): Experiments and performance analysis in support of 16-channel airborne X-band SAR data. *IEEE Trans. Geosci. Remote Sens.* **2021**, *59*, 6784–6798. [[CrossRef](#)]
35. Bordoni, F.; Krieger, G. Radiometric degradation associated with terrain height variations and pulse duration in scan-on-receive SAR images. *IEEE Trans. Geosci. Remote Sens.* **2022**, *60*, 5223214. [[CrossRef](#)]
36. Moreira, A.; Huang, Y. Airborne SAR processing of highly squinted data using a chirp scaling approach with integrated motion compensation. *IEEE Trans. Geosci. Remote Sens.* **1994**, *32*, 1029–1040. [[CrossRef](#)]
37. Dadi, M.; Donghui, H.U.; Chibiao, D. A new approach to airborne high resolution SAR motion compensation for large trajectory deviations. *Chin. J. Electron.* **2012**, *21*, 764–769.
38. Lu, Q.; Gao, Y.; Huang, P.; Liu, X. Range- and aperture-dependent motion compensation based on precise frequency division and chirp scaling for synthetic aperture radar. *IEEE Sens. J.* **2019**, *19*, 1435–1442. [[CrossRef](#)]
39. Yang, M.; Zhu, D. Efficient space-variant motion compensation approach for ultra-high-resolution SAR based on subswath processing. *IEEE J. Sel. Top. Appl. Earth Observ. Remote Sens.* **2018**, *11*, 2090–2103. [[CrossRef](#)]
40. Yan, Y.; He, Z.; Shi, C. A review on ISAR motion compensation techniques. In Proceedings of the 2017 2nd International Conference on Frontiers of Sensors Technologies, ICFST 2017, Shenzhen, China, 14–16 April 2017; pp. 340–344.
41. Lazarov, A.; Minchev, C. ISAR geometry, signal model and image processing algorithms. *IET Radar Sonar Navig.* **2017**, *11*, 1425–1434. [[CrossRef](#)]
42. Kim, J.W.; Kim, S.; Cho, H.; Song, W.-Y.; Yu, J.-W. Fast ISAR motion compensation using improved stage-by-stage approaching algorithm. *J. Electromagn. Waves Appl.* **2021**, *35*, 1587–1600. [[CrossRef](#)]
43. Chen, Z.; Zhang, Z.; Zhou, Y.; Wang, P.; Qiu, J. A novel motion compensation scheme for airborne very high resolution SAR. *Remote Sens.* **2021**, *13*, 2729. [[CrossRef](#)]
44. Wahl, D.E.; Eichel, P.H.; Ghiglia, D.C.; Jakowatz, C.V. Phase gradient autofocus—a robust tool for high resolution SAR phase correction. *IEEE Trans. Aerosp. Electron. Syst.* **1994**, *30*, 827–835. [[CrossRef](#)]
45. Zhang, G.; Liang, Y.; Suo, Z.; Xing, M. Modified ERMA with generalized resampling for maneuvering highly squinted TOPS SAR. *IEEE Geosci. Remote Sens. Lett.* **2022**, *19*, 1–5. [[CrossRef](#)]
46. Li, H.; Suo, Z.; Zheng, C.; Zhang, J.; Li, Z. An improved imaging algorithm for airborne near-nadir Tops SAR with yaw angle error. In Proceedings of the 2020 IEEE International Geoscience and Remote Sensing Symposium, IGARSS 2020, Waikoloa, HI, USA, 26 September–2 October 2020; pp. 2113–2116.
47. Fjortoft, R.; Gaudin, J.M.; Pourthie, N.; Lalaurie, J.-C.; Mallet, A.; Nouvel, J.-F.; Martinot-Lagarde, J.; Oriot, H.; Borderies, P.; Ruiz, C. KaRIn on SWOT: Characteristics of near-nadir Ka-band interferometric SAR imagery. *IEEE Trans. Geosci. Remote Sens.* **2014**, *52*, 2172–2185. [[CrossRef](#)]
48. Zhang, Z.; Xing, M.; Ding, J.; Bao, Z. Focusing parallel bistatic SAR data using the analytic transfer function in wavenumber domain. *IEEE Trans. Geosci. Remote Sens.* **2007**, *45*, 3633–3645. [[CrossRef](#)]